Available online at www.sciencedirect.com

ScienceDirect

Geochimica et Cosmochimica Acta 194 (2016) 211–232

Geochimica et Cosmochimica Acta

www.elsevier.com/locate/gca

The impact of electrogenic sulfur oxidation on the biogeochemistry of coastal sediments: A field study

Sebastiaan van de Velde [a,*], Ludovic Lesven [b], Laurine D.W. Burdorf [c], Silvia Hidalgo-Martinez [c], Jeanine S. Geelhoed [c], Pieter Van Rijswijk [c], Yue Gao [a], Filip J.R. Meysman [c,a]

[a] *Department of Analytical, Environmental and Geo-Chemistry, Vrije Universiteit Brussel (VUB), Pleinlaan 2, 1050 Brussel, Belgium*
[b] *LASIR Laboratory, University of Lille 1 (S&T), Cité Scientifique, 59655 Villeneuve d'Ascq, France*
[c] *Department of Ecosystem Studies, The Royal Netherlands Institute of Sea Research (NIOZ), Korringaweg 7, 4401 NT Yerseke, The Netherlands*

Received 9 June 2015; accepted in revised form 28 August 2016; available online 12 September 2016

Abstract

Electro-active sediments distinguish themselves from other sedimentary environments by the presence of microbially induced electrical currents in the surface layer of the sediment. The electron transport is generated by metabolic activity of long filamentous cable bacteria, in a process referred to as electrogenic sulfur oxidation (e-SOx). Laboratory experiments have shown that e-SOx exerts a large impact on the sediment geochemistry, but its influence on the *in situ* geochemistry of marine sediments has not been previously investigated. Here, we document the biogeochemical cycling associated with e-SOx in a cohesive coastal sediment in the North Sea (Station 130, Belgian Coastal Zone) during three campaigns (January, March and May 2014). Fluorescence *in situ* hybridization showed that cable bacteria were present in high densities throughout the sampling period, and that filaments penetrated up to 7 cm deep in the sediment, which is substantially deeper than previously recorded. High resolution microsensor profiling (pH, H_2S and O_2) revealed the typical geochemical fingerprint of e-SOx, with a wide separation (up to 4.8 cm) between the depth of oxygen penetration and the depth of sulfide appearance. The metabolic activity of cable bacteria induced a current density of 25–32 mA m^{-2} and created an electrical field of 12–17 mV m^{-1} in the upper centimeters of the sediment. This electrical field created an ionic drift, which strongly affected the depth profiles and fluxes of major cations (Ca^{2+}, Fe^{2+}) and anions (SO_4^{2-}) in the pore water. The strong acidification of the pore water at depth resulted in the dissolution of calcium carbonates and iron sulfides, thus leading to a strong accumulation of iron, calcium and manganese in the pore water. While sulfate accumulated in the upper centimeters, no significant effect of e-SOx was found on ammonium, phosphate and silicate depth profiles. Overall, our results demonstrate that cable bacteria can strongly modulate the sedimentary biogeochemical cycling under *in situ* conditions.

Keywords: Electrogenic sulfur oxidation; Marine sediments; Long-distance electron transport; Redox cycling; Cable bacteria

1. INTRODUCTION

Coastal sediments and continental shelves represent less than 20% of the seafloor surface, but account for more than 60% of the total organic matter mineralization in marine sediments (Burdige, 2006; Dunne et al., 2007). In coastal

* Corresponding author.
E-mail address: sevdevel@vub.ac.be (S. van de Velde).

http://dx.doi.org/10.1016/j.gca.2016.08.038
0016-7037/

and shelf sediments, sulfate reduction forms the dominant degradation pathway of organic matter, which results in the release of free sulfide in the pore water (Jorgensen, 1982; Aller, 2014). Despite a high production rate, little free sulfide is transferred across the sediment–water interface, due to efficient sulfide oxidation mechanisms, thus stimulating intense sulfur cycling within the sediment. It has been estimated that 75–90% of the free sulfide is reoxidized by various electron acceptors, such as oxygen, nitrate, and iron and manganese (hydr)oxides, while only a minor part of the free sulfide that is produced will precipitate as iron sulfides and becomes ultimately buried as pyrite (Bottrell and Newton, 2006).

Recently, a new mechanism of sulfide oxidation has been discovered in coastal sediments, in which the two half-reactions of sulfide oxidation are coupled by electrical currents that run over centimeter-scale distances (Nielsen et al., 2010). This process is referred to as electrogenic sulfur oxidation, abbreviated as e-SOx (Meysman et al., 2015), and couples the cathodic reduction of oxygen (COR) near the sediment–water interface to anodic sulfide oxidation (ASO) in deeper sediment layers (Nielsen et al., 2010; see schematic in Fig. 1d). Although conventional mechanisms for microbially induced electron transport, such as the use of redox shuttles, conductive pili (Gorby et al., 2006; Lovley, 2008; Logan and Rabaey, 2012) or conductance within the mineral matrix (Ntarlagiannis et al., 2007; Kato et al., 2010) cannot be completely excluded based on the observed sediment pore water chemistry in electro-active sediments, perturbation experiments (placing filters in the sediment, passing a tungsten wire through the suboxic zone) have provided strong evidence that long filamentous bacteria, so-called cable bacteria, are the most likely mediators of the observed long-distance electron transport (Pfeffer et al., 2012; Trojan et al., 2016). In laboratory incubation experiments, the depth distribution of these cable bacteria closely follows the development of the suboxic zone, thus providing additional evidence that cable bacteria are responsible for e-SOx (Schauer et al., 2014).

An electro-active sediment is a deposit that is subject to long-distance electron transport. This transport of electrons over centimeter-scale distances generates a charge separation, which will induce an electrical field in the pore water (Risgaard-Petersen et al., 2012). This electrical field will exert a force on the ions in the pore water, thus generating an additional advective solute transport termed "ionic drift" (Risgaard-Petersen et al., 2012). Recently, a new micro-electrode has been developed which senses the electrical potential that accompanies the electrical field and current (Damgaard et al., 2014). These measurements reveal that the current density can amount up to 400 mA m^{-2} (Risgaard-Petersen et al., 2014), which then generates substantial fluxes due to ionic drift in the electro-active zone of the sediment (i.e. the zone where cable bacteria are active).

The discovery that sediments can be electro-active has the potential to radically change our view of redox pathways and geochemical cycling in coastal sediments. Laboratory incubation experiments have shown that e-SOx has the capacity to exert a strong influence on the carbon, iron and sulfur cycling in marine sediments (Risgaard-Petersen et al., 2012; Rao et al., 2016). This strong effect is particularly induced by the spatial separation of strong proton production and strong proton consumption, respectively associated with the ASO half-reaction at depth (Fig. 1d) and the COR half-reaction near the sediment surface (Fig. 1d). The release of protons in the suboxic zone promotes the dissolution of iron sulfide, which makes free sulfide available for oxidation by e-SOx, which again releases more protons, thus creating a positive feedback mechanism (Risgaard-Petersen et al., 2012; Meysman et al., 2015). Similarly, Ca^{2+} is liberated from carbonate minerals by acidic dissolution at depth, and upon upward diffusion, these Ca^{2+} ions re-precipitate as calcium carbonate near the sediment–water interface (SWI), where alkaline conditions prevail (Risgaard-Petersen et al., 2012). Moreover, a recent study has shown that the development of e-SOx strongly stimulates solute fluxes across the sediment–water interface, and is capable of releasing large amounts of alkalinity in the overlying water (Rao et al., 2016).

Originally discovered within laboratory incubations, it has been recently demonstrated that e-SOx occurs in a variety of natural environments like coastal mud plains, sat marshes, seasonally hypoxic basins, and mangroves (Malkin et al., 2014; Burdorf et al., 2016). However, until now, the geochemical impact of e-SOx on the geochemistry of *in situ* sediments has not been documented. In this study, we examined the effect of e-SOx on the cycling of carbon, nutrients, metals and sulfur in muddy sediment of the Belgian Coastal Zone.

2. MATERIALS AND METHODS

2.1. Field site location

Sediment biogeochemistry was investigated at Station 130 (51°16.3′N, 2°54.3′E), a subtidal mud accumulation site located in the Belgian Coastal Zone (BCZ) of the southern North Sea (Fig. 1a and b), located ~5 km offshore from the coastal city of Oostende (Belgium). This site is characterized by an average water depth of ~12 m, a tidal amplitude of ~4.5 m and strong tidal currents parallel to the coast (Vlaamse Hydrografie, 2012). The sediment at the field site predominantly consists of cohesive clay and mud, sometimes covered by a thin (0–2 cm) sand layer. The sediment is rich in organic matter and carbonate (Van Lancker et al., 2004), has a shallow oxygen penetration depth (1–3 mm) (Gao et al., 2009) and large bioturbating fauna are largely absent (Braeckman et al., 2014). A previous study has documented the geochemical fingerprint of e-SOx as well as the presence of cable bacteria on two separate occasions at this site (October 2011 and March 2013; Malkin et al., 2014), but no detailed pore water investigations were carried out.

2.2. Sediment sampling

Bottom water samples and sediment cores were collected in January, March and May 2014. Temperature (T), salinity (S) and oxygen (O_2) saturation were measured in the bot-

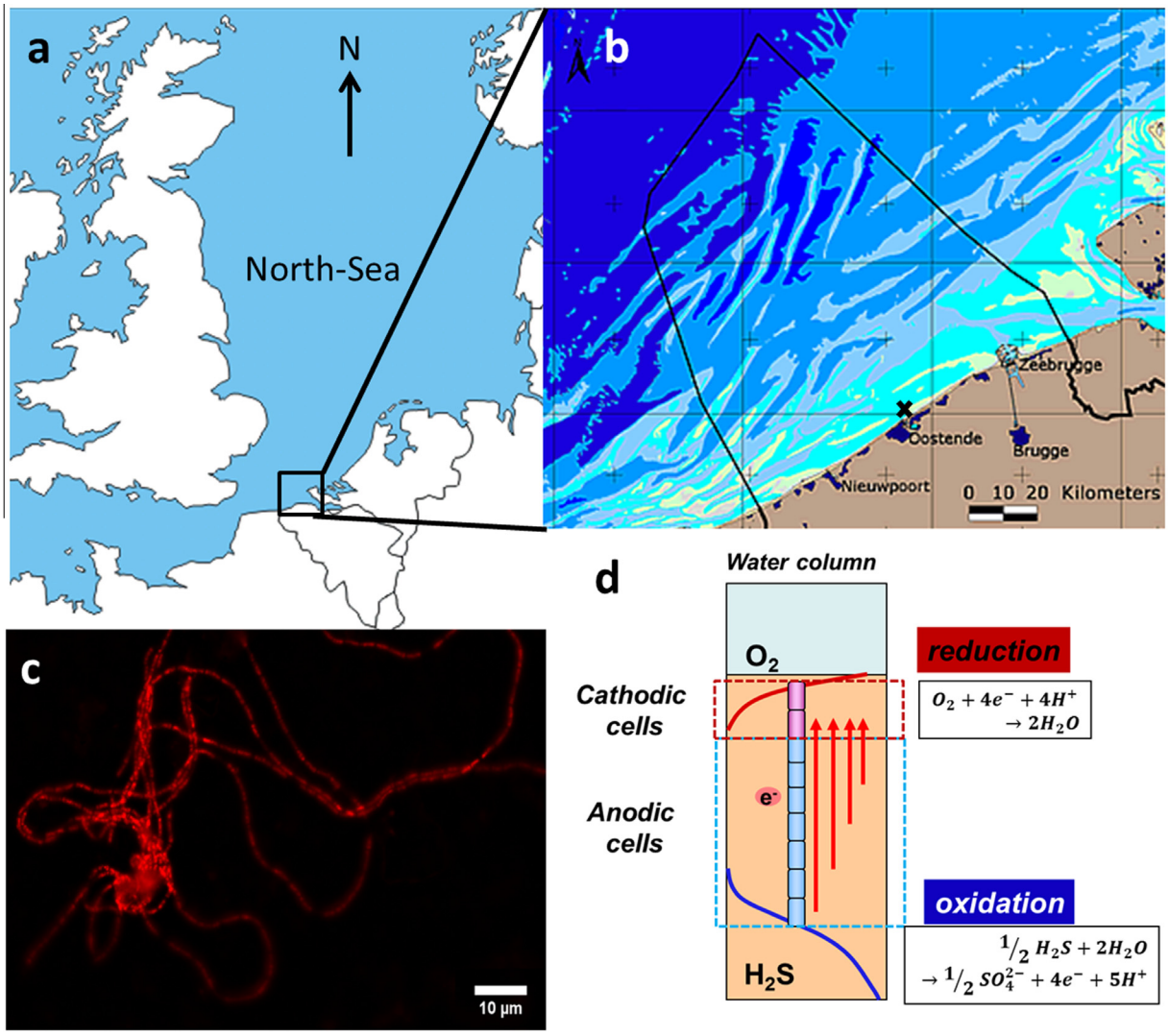

Fig. 1. (a) Overview map of the southern North Sea. (b) Detailed bathymetry map of the Belgian exclusive economic zone in the Southern North Sea (blue line). The black marker indicates the field site (Station 130; N 51°16.3′, E 2°54.3′). (c) Microscopic image obtained by Fluorescence *In Situ* Hybridization (probe DSB706) of a cable bacteria fragment from the field site. (d) A schematic of electrogenic sulfur oxidation (e-SOx) by cable bacteria (see Meysman et al., 2015 for further details). Electrons are supplied by anodic sulfide oxidation in deeper sediment layers, subsequently transported along the longitudinal axis of the cable bacteria, and finally captured again by cathodic oxygen reduction near the sediment surface. (For interpretation of the references to colour in this figure legend, the reader is referred to the web version of this article.)

tom water at ~2 m above the seafloor with a CTD (Seabird 19plusV2, USA). Bottom water was sampled with 5 L NISKIN bottles attached to a CTD carrousel instrument (Seabird 55 ECO, USA). Bottom water was analyzed for O_2, cations (Ca^{2+}, Mg^{2+}, Fe^{2+}, Mn^{2+}), anions (SO_4^{2-}), nutrients (NO_3^- NO_2^-, NH_4^+, H_4SiO_4, PO_4^{3-}), dissolved inorganic carbon (DIC) and total alkalinity (A_T).

During each campaign, 12 sediment gravity cores were collected (UWITEC, Austria) using transparent PVC core liners (60 mm inner diameter; 60 cm long). Upon retrieval, cores were carefully inspected and only those with a visually undisturbed sediment surface were retained for further study. Cores were transported back to the shore-based laboratory in an insulated container (transit time ~2 h). Upon arrival at the laboratory, the cores were inspected again for signs of disturbance, and 6 were selected for microsensor profiling analysis (see Section 2.3), which started within 4 h after sampling. After microsensor profiling, the cores were left overnight in an incubation tank, which was located in a climate-controlled room at *in situ* temperature and filled with air-saturated water collected from the sampling site.

The next day, 2 cores were randomly selected from the 6 cores that were microsensor profiled the day before and sectioned for pore water extraction in an anaerobic glove box (N_2 atmosphere; Coy lab products, USA). Slicing occurred at 0.5 cm resolution from 0 to 5 cm depth, at 1 cm resolution between 5 and 10 cm depth, and in 2 cm slices from 10 to 16 cm depth. Sediment sections were collected in 50 ml centrifuge tubes (polypropylene; TPP, Switzerland)

and centrifuged at 4000*g* for 7.5 min (Sigma 3-18KS, Sigma Laborzentrifugen GmbH, Germany). Subsequently, the centrifuge tubes were opened in the anaerobic glove box and overlying pore water was transferred into suitable sample containers after filtration through 0.22 μm cellulose acetate filters (Chromafil Xtra). Pore water samples were analyzed for the same dissolved analytes as the bottom water. The solid phase that remained after centrifugation was freeze-dried and ground manually with a pestle and mortar for solid phase analysis and *aqua regia* extraction. The solid phase analysis provided the elemental composition (total organic carbon, total inorganic carbon and total nitrogen), while the *aqua regia* extraction provided the extractable iron and manganese content of the sediment.

Two additional cores (also randomly selected from the 6 that were microsensor profiled) were subsampled for analysis of elemental sulfur (S^0) and acid volatile sulfide (AVS). These cores were also sectioned in the anaerobic glove box and at the same depth resolution as described above. Sediment slices were mixed and approximately 1 g was transferred into a 50 ml centrifuge tube containing 3 mL of zinc acetate (20%) for S^0 extraction and the rest into an airtight sealed aluminum bag, which was flash-frozen in liquid nitrogen as preservation for later AVS analysis.

The remaining 2 cores were sliced outside the glove box for porosity and solid phase density determinations, while a 0.5 cm^3 of wet sediment subsample was taken (after homogenization) from each slice and fixed with 0.5 mL of ethanol (99.8% molecular grade). This subsample was cooled at −20 °C and used for fluorescence *in situ* hybridization (see Section 2.9).

2.3. Microsensor profiling

Microsensor profiling was carried out using commercial micro-electrodes (Unisense A.S., Denmark) for dissolved H_2S (100 μm tip diameter), O_2 (100 μm tip) and pH (200 μm tip) on 6 replicate cores. In each core, 2 replicate profiles were taken for each of the three parameters. For pH, a 3 point calibration was made using standard NBS buffers (pH = 4, 7, 10), followed by a salinity correction with TRIS buffer (Dickson et al., 2007). pH measurements were performed using an external Ag/AgCl/[KCl] = 3 M reference electrode (Radiometer) and values are reported on the total pH scale. For dissolved H_2S, a 5 point standard calibration curve was made using Na_2S standards, which were freshly prepared before each sampling campaign. Total sulfide concentration ($\sum H_2S = [HS^-] + [H_2S]$) was calculated from the dissolved H_2S concentration based on the pH measured at the same depth using the relations of Millero et al. (1988) for the thermodynamic equilibrium constant of H_2S. For O_2, a 2-point calibration was made using air-saturated seawater (100% saturation) and the anoxic zone of the sediment (0% saturation).

2.4. Physical sediment parameters

Sediment grain size and sorting were measured in January 2014 by laser diffraction using a Malvern Mastersizer 2000 (McCave, 1986), after homogenizing freeze-dried sediment from the top 5 cm. The solid phase density was determined by adding a known mass of grinded, freeze-dried sediment to a 100 ml graduated cylinder filled with tap water and recording the volume displacement. Sediment porosity (volume of pore water per total volume of sediment) was determined from water content and solid phase density measurements, considering the salt content of the pore water. The water content was determined as the volume of water removed when wet sediment samples were dried to constant weight at 60 °C.

2.5. Bottom water analysis

Samples for major dissolved cations (Ca^{2+}, Mg^{2+}, Fe^{2+}, Mn^{2+}) analysis were immediately stabilized with 50 μL/mL bidistilled HNO_3 (65%, suprapure, Merck) and stored at 4 °C. Prior to analysis, these samples were mixed with a standard matrix solution containing 35 salinity artificial seawater, 2% HNO_3 and 0.2 mg L^{-1} Ytterbium as an internal standard (Crompton, 1989). Samples were diluted 50 times and subsequently analyzed by Inductively Coupled Plasma – Optical Emission Spectroscopy (ICP-OES, ThermoFisher iCAP6500); precision was <2% for all analytes. From here on, we will refer to dissolved iron as Fe^{2+}, though it should be noted that ICP-OES measures the total dissolved concentration of iron. Accordingly, samples may also contain colloidal Fe^{3+} in addition to ferrous iron (Fe^{2+}), but in general the Fe^{3+} contribution is negligible (Viollier et al., 2000). Similarly, dissolved manganese is referred to as Mn^{2+}, but may also consist of smaller amounts of Mn^{3+} and Mn^{4+} (Madison et al., 2011).

Samples for SO_4^{2-} analysis were diluted 10 times, and separated by ion chromatography, using an isocratic eluent (3.5 mM Na_2CO_3/1 mM $NaHCO_3$) combined with Dionex AS-14 analytical column (Thermo Scientific). Quantification was done by a conductivity detector (ED40 electrochemical detector) (Gros et al., 2008) with a precision of 8%.

Nutrient samples (NH_4^+, H_4SiO_4, NO_3^-, NO_2^-) were diluted 25 times with a low nutrient containing seawater matrix solution and analyzed by a SEAL QuAAtro segmented flow analyzer (Aminot et al., 2009). Samples for phosphate (PO_4^{3-}) analysis were collected in a separate vial, acidified with 100 μL/mL H_2SO_4 (1 M) and also analyzed by the SEAL QuAAtro system. Precision was <4% for all analytes.

Samples for DIC analysis were collected in 5 mL headspace vials, left to overflow and poisoned with 10 μL of a saturated $HgCl_2$ solution. Bottom water DIC analysis was performed using an AS-C3 analyzer (Apollo SciTech, USA), which consists of an acidification and purging unit in combination with a LICOR-7000 CO_2/H_2O Gas Analyzer (precision 0.3%). Quality assurance was done by regular analysis of Certified Reference Materials (CRM) obtained from the Scripps Institution of Oceanography (Batch 140; Dickson et al., 2003).

2.6. Pore water analysis

Pore water analysis was identical as for the bottom water for all analytes apart from DIC and A_T. Pore water

samples for DIC analysis were collected in 350 µL headspace vials and poisoned with 2 µL of saturated $HgCl_2$. Pore water DIC analysis was performed using a Segmented Flow Analyser (San++ SKALAR) according to the method of Stoll et al. (2001) (precision 3%). Quality assurance involved regular analysis of Certified Reference Materials (CRM) which were obtained from the Scripps Institution of Oceanography (batch 140; Dickson et al., 2003).

Pore water A_T was determined using the standard operating procedure for open cell potentiometric titration (Dickson et al., 2007, SOP 3b), using a manual titrator (Metrohm 775 Dosimat), a high accuracy burette (1 ± 0.001 mL) and a combined pH glass electrode (Orion 8103BN ROSS, Thermo Scientific) (precision 2%). Temperature was monitored during the measurements. A_T values were calculated by a non-linear least-squares fit to the titration data (Dickson et al., 2007, SOP 3b) in a custom-made script in the open source programming framework R. Quality assurance involved regular analysis of Certified Reference Materials (CRM) which were obtained from the Scripps Institution of Oceanography (Dickson et al., 2003).

Note that due to the high DIC and A_T concentrations in the pore water (up to 20 mM), the CRM material provided by the Scripps Institution of Oceanography provides only a suitable quality check in the lower concentration range. For the higher concentration range, no standardized quality control procedure is currently available.

2.7. Solid phase analysis

For the analysis of particulate organic carbon (POC), particulate inorganic carbon (PIC) and total nitrogen (TN), sediment samples were freeze-dried, ground to a fine powder and analyzed by an Interscience Flash 2000 organic element analyzer. Before the analysis, samples for POC were first acidified with 0.1 M HCl to remove the inorganic carbon, and PIC was subsequently calculated by the difference between total carbon and POC (Nieuwenhuize et al., 1994). Concentrations of POC and PIC are expressed as mass% of dry sediment. The C:N ratio of the organic matter in the sediment was calculated as the ratio of POC over TN. Precision was <5% for the TC, POC measurements and TN measurements.

To determine the solid phase content of iron and manganese, sediment samples were freeze-dried and ground to a fine powder for microwave assisted digestion (CEM Mars 5) using *aqua regia* as extraction agent (ISO 12914:2012). Subsequently, samples were analyzed by ICP-OES (ThermoFisher iCAP6500) after 100 times dilution in a standard matrix solution with a 1/3 ratio of HNO_3/HCl using 0.2 ppm Ytterbium as internal reference standard (Poussel et al., 1993) (precision was 1% for Fe and 2% for Mn resp.).

Prior to elemental sulfur (S^0) analysis, H_2S was removed from the 1 g of wet sediment sample by adding 3 mL zinc acetate (ZnAc, 20%, w/v) solution. Before extraction, the sample was centrifuged and the ZnAc supernatant was discarded. Subsequently, 20 mL of methanol (MeOH, 100%) was added and the mixture was left to shake for 12 h. Afterwards, the mixture was centrifuged and the supernatant was analyzed with high performance liquid chromatography (HPLC) – UV detector ($\lambda = 265$ m). The eluent was methanol with a flow regime of one 100% isocratic step (precision 6%).

Acid-volatile sulfide (AVS) was determined after its conversion into H_2S gas by the extraction procedure described by Canfield et al. (1986) and Cornwell and Morse (1987). It is assumed that S^0 is not extracted in this step (Burton et al., 2008). Briefly, 1 g of wet sediment was transferred from the sealed aluminum bag (see Section 2.2) to a distillation flask in a glove box previously flushed with nitrogen. Then, AVS was extracted with a 6 M HCl solution during 1 h under nitrogen atmosphere in a reactor, equipped with a stir bar. The formed gas H_2S is purged from solution using N_2 as carrier gas and trapped in 20 mL of 1 M EDTA-NaOH solution and subsequently titrated by potentiometry with a Cd^{2+} standard solution (100 mg L^{-1}) using a sulfide ion selective electrode (Orion) and a $Hg/Hg_2/[SO_4^{2-}] = 3$ M reference electrode (precision was <10%). Concentrations of total Fe, total Mn, S^0 and AVS are expressed as µmol g^{-1} of dry sediment.

2.8. Flux analysis and rate estimation

The Diffusive Oxygen Uptake (DOU) of the sediment was calculated from the oxygen microsensor depth profiles, using Fick's first law:

$$J = \frac{\varphi}{\theta^2} D_0(S,T) \frac{\partial C}{\partial x} \quad (1)$$

where J is the influx of oxygen, C is the oxygen concentration in the pore water, x is the depth into the sediment, φ represents porosity, and θ^2 is the correction factor for sediment tortuosity ($\theta^2 = 1 - 2\ln(\varphi)$) (Boudreau and Meysman, 2006). The molecular diffusion coefficient is calculated for measured salinity and temperature using the R package CRAN: marelac (Soetaert et al., 2010), which is based on the constitutive relations presented in Boudreau (1997). The concentration gradient, $\partial C/\partial x$, was calculated by the linear regression from the concentration profile right below the sediment–water interface (SWI).

Production and consumption rates of DIC, NH_4^+, PO_4^{3-}, SO_4^{2-}, Fe^{2+}, Mn^{2+} and Ca^{2+} were calculated using the PROFILE software (Berg et al., 1998), while specifically accounting for ionic drift in the electro-active zone of the sediment. This approach is further detailed in Appendix A. The current density (i.e. the current per unit of sediment area) and cathodic oxygen consumption (COC) were estimated from the alkalinity production and consumption associated with the redox half-reactions of e-SOx (Fig. 1d). The imposed electrical field was calculated from the estimated current densities. These procedures are explained in detail in Appendix B.

2.9. Fluorescence *in situ* hybridization

The abundance and depth distribution of cable bacteria was determined via Fluorescence *In Situ* Hybridisation (FISH) on subsamples fixed with ethanol and

stored at −20 °C. The FISH procedure follows the protocol as described in detail in Vasquez-Cardenas et al. (2015). The DSB706 probe was used, which targets the Desulfobulbaceae (Manz et al., 1992) to which the cable bacteria are affiliated. Samples were counterstained with DAPI (4′,6-diamidino-2-phenylindole) and the samples from the top 5 cm were analyzed at 0.5 cm intervals. When cable bacteria were present, deeper layers were also analyzed, until a depth where cable bacteria were no longer found.

2.10. Statistics

Statistical analyses were carried out with the R-package CRAN:stats. To compare the mean of two sets, the Welch two-sample *t*-test was used. The null-hypothesis was rejected when the calculated *p*-value was above the threshold $p > 0.05$. These tests have been used to compare the values of the geochemical fingerprint of e-SOx (see Table 1) obtained by microsensor profiling.

3. RESULTS

3.1. Bottom water conditions and general sediment appearance

Over the four month sampling period, the bottom water temperature increased from 7.44 ± 0.02 °C in January 2014 to 15.81 ± 0.05 °C in May 2014, while salinity remained constant at ~33.7 (Table 1). The CTD profiles did not show any trend with water depth (data not shown), indicating that the water column was fully mixed, which is characteristic for the southern North Sea throughout the whole year. The O_2 saturation and pCO_2 showed an inverse relation (Table 1). In March, the bottom water was oversaturated in O_2 and strongly undersaturated in CO_2 with respect to the atmosphere, most likely due to the spring phytoplankton bloom. The nutrient concentrations were very low in May ($NH_4^+ < 0.3$ μM, $NO_3^- < 0.15$ μM; $PO_4^{3-} < 0.01$ μM), also suggesting nutrient depletion due to previous primary production.

Table 1
Summary of the bottom water conditions, and geochemical parameters and rates estimated in three months (January, March and May 2014). NA: values not available. Uncertainty represent the standard deviation (s.d) of replicate samples. Values for temperature, salinity and oxygen saturation are provided as the (mean ± 1 s.d.) of the CTD recordings. Other values represent the (mean ± 1 s.d.) of replicate samples/cores. Values without standard deviation are from single samples/cores.

Parameter	Symbol	Units	January	March	May
Bottom water conditions					
Temperature	T	°C	7.44 ± 0.02	9.32 ± 0.09	15.81 ± 0.05
Salinity	S	–	33.7 ± 0.2	33.4 ± 0.1	34.0 ± 0.2
Oxygen saturation	–	%	90.6 ± 3.1	109.9 ± 4.9	80.5 ± 4.7
Partial CO_2 pressure	pCO_2	μM	821	251	487
DIC concentration	–	mM	NA	2.178 ± 0.005	2.02 ± 0.06
NH_4^+ concentration	–	μM	NA	0.41 ± 0.07	0.31 ± 0.02
NO_3^- concentration	–	μM	NA	12.5 ± 0.1	0.15 ± 0.01
NO_2^- concentration	–	μM	NA	0.26 ± 0.01	0.01 ± 0.01
PO_4^{3-} concentration	–	μM	NA	0.14 ± 0.01	0.01 ± 0.01
H_4SiO_4 concentration	–	μM	NA	0.06 ± 0.01	0.08 ± 0.01
SO_4^{2-} concentration	–	mM	27.2 ± 0.7	25.40 ± 0.01	27.3 ± 0.5
Nutrient regeneration					
DIC production	–	mmol m^{-2} d^{-1}	64 ± 25	46.1 ± 8.9	24 ± 13
NH_4^+ production	–	mmol m^{-2} d^{-1}	4.8 ± 1.0	4.8 ± 0.7	2.8 ± 0.1
PO_4^{3-} production	–	mmol m^{-2} d^{-1}	0.25 ± 0.01	NA	0.19 ± 0.02
SO_4^{2-} consumption	–	mmol m^{-2} d^{-1}	18.0 ± 3.3	22.7 ± 1.7	12.3 ± 5.3
H_4SiO_4 production	–	mmol m^{-2} d^{-1}	0.4 ± 0.3	0.81 ± 0.08	0.6 ± 0.9
Geochemical fingerprint e-SOx					
Oxygen penetration depth	OPD	mm	2 ± 1	2.0 ± 0.4	2.3 ± 0.4
Sulfide Appearance Depth	SAD	cm	2.5 ± 0.5	5.0 ± 1.4	2.6 ± 0.8
Diffusive Oxygen Uptake	DOU	mmol m^{-2} d^{-1}	13.2 ± 4.0	14.5 ± 3.9	16.8 ± 5.5
pH minimum	–	–	6.35 ± 0.25	6.54 ± 0.14	6.38 ± 0.25
Depth of pH minimum	–	cm	2.07 ± 0.27	3.88 ± 0.72	3.05 ± 0.49
Electrical network properties					
Current density oxic zone	–	mA m^{-2}	27.1	NA	25 ± 19
Current density anoxic zone	–	mA m^{-2}	31.7	NA	26.3 ± 4.3
O_2 consumed by COR	p	%	50 ± 16	NA	34 ± 28
Conductivity pore water	σ_{PW}	S m^{-1}	3.45	3.59	4.26
Electrical field	E	mV m^{-1}	16.9 ± 1.9	NA	11.9 ± 0.4
Integrated filament density	–	m cm^{-2}	186	352	168

The sediment appearance and coloration were similar in the three campaigns. The first 1–2 mm of the sediment had a light brown color, which was followed by a grey zone, extending over 5–10 cm deep. This grey zone turned gradually darker towards deeper depths. During core slicing, there were no macrofauna or burrows observed, indicating that the sampling site had a low level of bioturbation, which is consistent with a recent, yearlong survey of the macrofauna at the field site (Braeckman et al., 2014). The top sediment had a solid phase density of 2.6 ± 0.4 g cm^{-3}, a median grain size of 28.7 μm, and more than 60% of the particles were finer than 63 μm, so the sediment can be classified as 'sandy mud' (Burdige, 2006).

The porosity depth profile was similar for all three sampled months, except for the top 2 cm, which showed strong fluctuations between months (Fig. 2). The analysis of two different cores gave nearly identical porosity depth profiles, suggesting that lateral heterogeneity in sediment was small at the field site. The profile in January had a low porosity (0.53) in the top 5 mm, due to a thin sand layer that was deposited on top of the sediment. Below, the porosity slightly declined with depth, decreasing from 0.78 at 2 cm depth to 0.73 at 10 cm depth (depth averaged value: 0.77 $\pm$ 0.01). In March, the top 5 mm had a higher porosity (0.84), but the depth horizon between 1 and 10 cm showed similar porosity values as in January. In May, the sediment porosity linearly decreased from the sediment surface down to 13 cm depth, a small sand layer (~5 mm) was however visible on top of the sediment. Note that the porosity profiles do not show the classical exponential decrease with depth as often encountered in coastal sediments (Boudreau et al., 1998). The absence of a strong depth gradient in porosity, combined with the relatively low porosity values for fine grained sediment, suggests that the sediment forms a relatively old, well compacted, consolidated deposit.

3.2. Microsensor profiling

Microsensor profiles (Fig. 3) showed a shallow Oxygen Penetration Depth (OPD; operationally defined as the depth where the oxygen concentration was <1 μM), which ranged from 1.9 ± 1.1 mm in January to 2.3 ± 0.4 mm in May (reported as mean $\pm$ standard deviation over 6 profiles; Table 1). There was no significant difference in the OPD between the three months. Note that the OPD in January has a much higher standard deviation, compared to the other two months, which was probably due to sample handling, as the cores where not kept submerged in air-saturated seawater during microsensor profiling. For the subsequent two campaigns, we adapted the sampling protocol, and cores were submerged in fully oxygenated seawater. As a result, the variability in OPD was strongly reduced in March and May.

Free sulfide ($\sum H_2S = [HS^-] + [H_2S]$) was generally undetectable in the first centimeters, and accumulated in deeper layers to only very low concentrations (~10 μM; Fig. 3). The Sulfide Appearance Depth (SAD, operationally defined as the first depth where sulfide reached concentrations >1 μM) was similar in January and May with the value of 2.5 ± 0.5 cm and 2.6 ± 0.7 cm respectively. However, the SAD was significantly deeper in March, when free sulfide remained undetectable in the first 5.0 ± 1.4 cm. Accordingly, in all three months a sizeable suboxic zone, operationally defined as the sediment horizon between OPD and SAD, was present (Table 1).

The pH depth profiles showed the characteristic geochemical fingerprint of e-SOx (Nielsen et al., 2010; Meysman et al., 2015) in January, with a pH maximum at the OPD, and a pH minimum near the SAD. However, no subsurface pH maxima were observed in March and May, though the low pH conditions near the SAD were sustained. The pH minimum was similar in January and March, 6.35 ± 0.25 and 6.38 ± 0.25 respectively, and was slightly higher in May (6.54 ± 0.14). This pH minimum is created by the anodic oxidation of sulfide (Eq. (B.1); Fig. 1d); hence, the depth where this minimum is achieved should be near the SAD. Comparison of depths showed that there was no significant difference between SAD and the depth of the pH minimum. Furthermore, all replicate pH profiles in May showed a marked inflection at ~5 mm depth, which coincided with the extent of a thin sand-layer (~5 mm) that was deposited on top of the sediment. As the effective diffusion coefficient can strongly change when moving from the surficial low-porosity sand layer to the underlying high-porosity clay layer, this could explain the observed "bump" in the profiles.

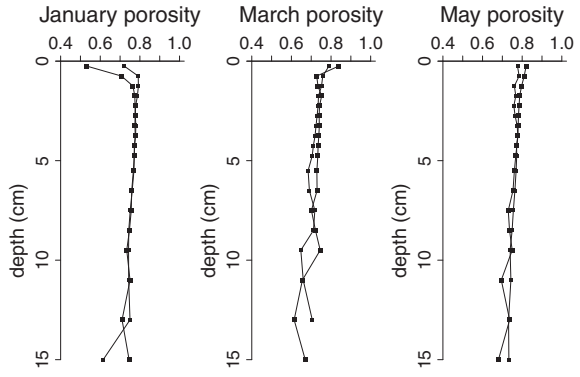

Fig. 2. Vertical depth profiles of porosity recorded in different months in 2014: (a) January, (b) March and (c) May. Depth profiles for two replicate sediment cores are shown.

3.3. Cable bacteria densities

The filament density of cable bacteria was determined by FISH as a function of depth, and showed a similar pattern at all three sampling times (Fig. 3). Cable bacteria were abundant throughout the oxic and suboxic zones, and are no longer present below the sulfide appearance depth. In January and May the highest filament densities were recorded between 5 and 10 mm, after which the filament densities decreased with depth. The filament density in the first half centimeter in May was only half of that in the subsequent layer, coinciding with the extent of the surficial sand layer that was deposited at that time.

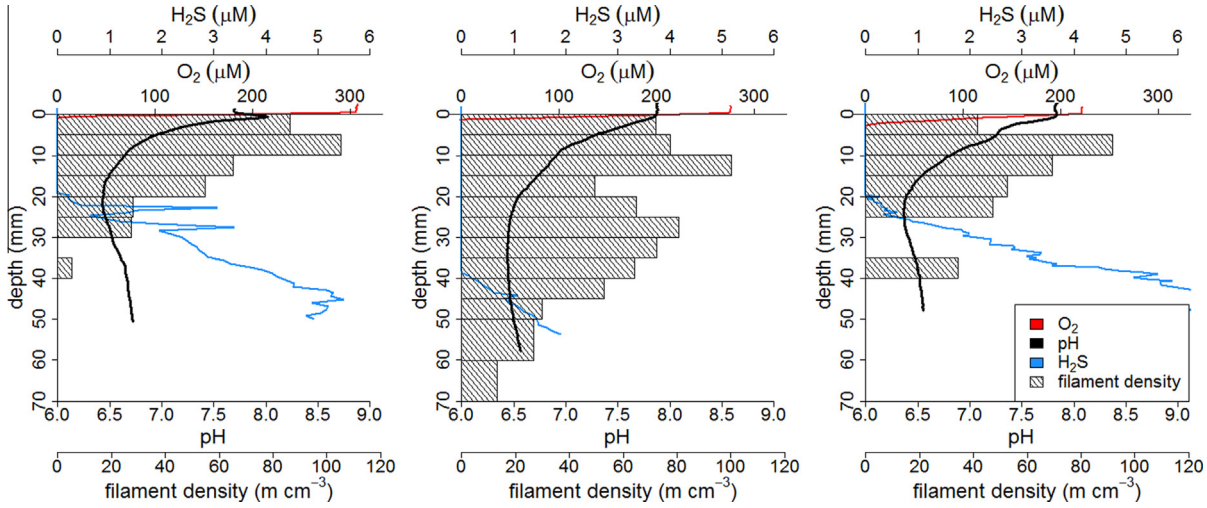

Fig. 3. Microsensor depth profiles of pH (black line), oxygen (red line) and total free sulfide (blue line) at the field site recorded in different months in 2014: (a) January, (b) March and (c) May. Profiles are shown for one representative core (out of 6 cores that were profiled in total). The shaded boxes denote the abundance of cable bacteria as determined by Fluorescence *In Situ* Hybridization (filament density is expressed in m of filaments per bulk sediment cm^{-3}). (For interpretation of the references to colour in this figure legend, the reader is referred to the web version of this article.)

When integrated over depth, the filament density was almost twice as high in March (352 m cm^{-2}), compared to January (186 m cm^{-2}) and May (168 m cm^{-2}) (Table 1). This coincided with the deep extension of the suboxic zone, as cable bacteria were found up to 70 mm deep in the sediment in March.

3.4. Solid phase chemistry

Solid phase analysis was carried out at the start (January) and end (May) of the sampling period (Fig. 4). The depth averaged value of particulate organic carbon (POC) was not significantly different in January ($1.61 \pm 0.53\%$) compared to May ($1.70 \pm 0.52\%$). The depth profile of POC in both months showed a clear depletion in the top 2–3 cm (POC $\sim 1.2 \pm 0.6\%$), whereas the profile remained constant from 3–16 cm (POC $\sim 1.9 \pm 0.3\%$). The depth profile of particulate inorganic carbon (PIC, assumed to mainly consist of $CaCO_3$) had a similar shape, i.e., constant with depth slightly lower content below the surface. After conversion of PIC values to $CaCO_3$ concentrations, the depth averaged $CaCO_3$ content in January ($28.3 \pm 1.9\%$) was not significantly different from May ($26.6 \pm 2.0\%$), and indicated that the sediment contained a sizeable carbonate fraction. The depth averaged C:N ratio in January (8.62 ± 0.39) was also not significantly different from May (8.48 ± 0.45), which suggests the organic matter is predominantly of marine origin. The depth profile of the C:N ratio was virtually constant, although a slight enrichment in carbon was observed in the top 2 cm in January.

The depth profiles of extractable iron and manganese were strongly correlated, and were also strikingly similar to the depth profile of particulate organic carbon. Solid phase iron and manganese showed depletion in the top few centimeters in both January and May, as well as a depleted horizon at ~9 cm depth in January (Fig. 4b).

AVS concentrations (Fig. 4c) were lowest at the SWI (~8 μmol g^{-1}) and quickly increased to a value of 21 ± 4 μmol g^{-1} (depth averaged over the 0–1.5 cm horizon) in January. In May, AVS showed a surface depletion in the top 2 cm (depth averaged value of 12 ± 2 μmol g^{-1}), followed by an enrichment between 2 cm and 3 cm depth (depth averaged value of 28 ± 5 μmol g^{-1}) and a subsequent decline (depth averaged value of 25 ± 4 μmol g^{-1} below 3 cm). The replicate core in May did not show the same strong enrichment of AVS at 3 cm depth, but did reveal the depletion zone in the surface layer and higher AVS concentrations in deeper sediment layers (data not shown).

Strikingly, concentrations of elemental sulfur (S^0) were of similar magnitude as AVS values. A clear enrichment of S^0 was observed in the upper sediment right below the SWI in both January and May (enrichment zone extending from 1 to 6 cm). Starting from a low value at the interface (3–8 μmol g^{-1}), values rapidly increased in the first two centimeters, to reach a maximum value of ~35 μmol g^{-1} at 3 cm depth in January, after which values decreased again and became constant with depth. In May, the enrichment zone had a lower inventory of S^0 than in January (Fig. 4c), which could indicate consumption during the preceding months.

3.5. Pore water geochemistry

Depth profiles of pore water solutes were determined in all three months (Fig. 5). These depth profiles were subsequently analyzed with the PROFILE software (Berg et al., 1998) to determine the apparent production and con-

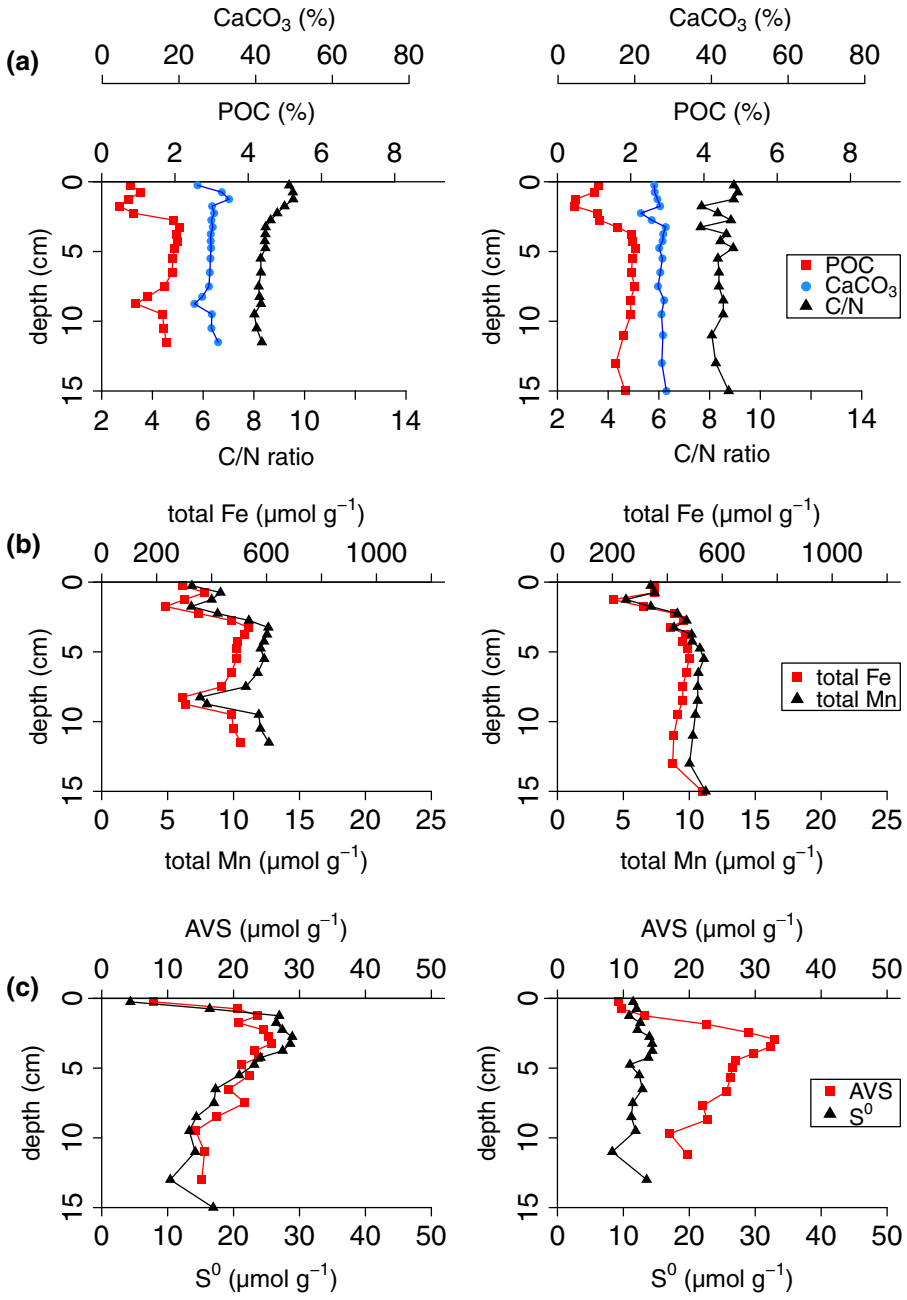

Fig. 4. Vertical depth profiles of solid phase compounds recorded at the field site in January (left column) and May 2014 (right column): calcium carbonate ($CaCO_3$), particulate organic carbon (POC), *C/N* ratio of organic matter, total extractable iron (total Fe), total extractable manganese (total Mn), acid volatile sulfide (AVS) and elemental sulfur (S^0). Concentrations are either expressed in µmol g^{-1} of dry sediment for total Fe, total Mn, S^0, AVS, and in mass% (gram per gram of dry sediment) for $CaCO_3$ and POC.

sumption rates (Fig. 6 shows representative example profiles).

Dissolved iron (Fe^{2+}), manganese (Mn^{2+}) and calcium (Ca^{2+}) showed a clear subsurface accumulation over the entire sampling period, suggesting strong mobilization and cycling in the surface sediment (Fig. 5a). The Fe^{2+} concentration stayed below the detection limit in the overlying water, but quickly increased in the sediment and reached a subsurface maximum of 0.5 mM at 3 cm depth in January and subsequently declined to 0.25 mM in deeper layers. In March, the subsurface Fe^{2+} maximum was flattened and extended deeper into the sediment in concert with the deepening of the suboxic zone (~0.6 mM over 2–6 cm). In contrast, the subsurface maximum showed a sharp peak with a peak concentration of ~1 mM at 3.5 cm depth in May. Towards deeper layers, the Fe^{2+} concentration decreased, but never became fully depleted in the pore water. PROFILE analysis (Fig. 6a) confirmed the strong mobilization

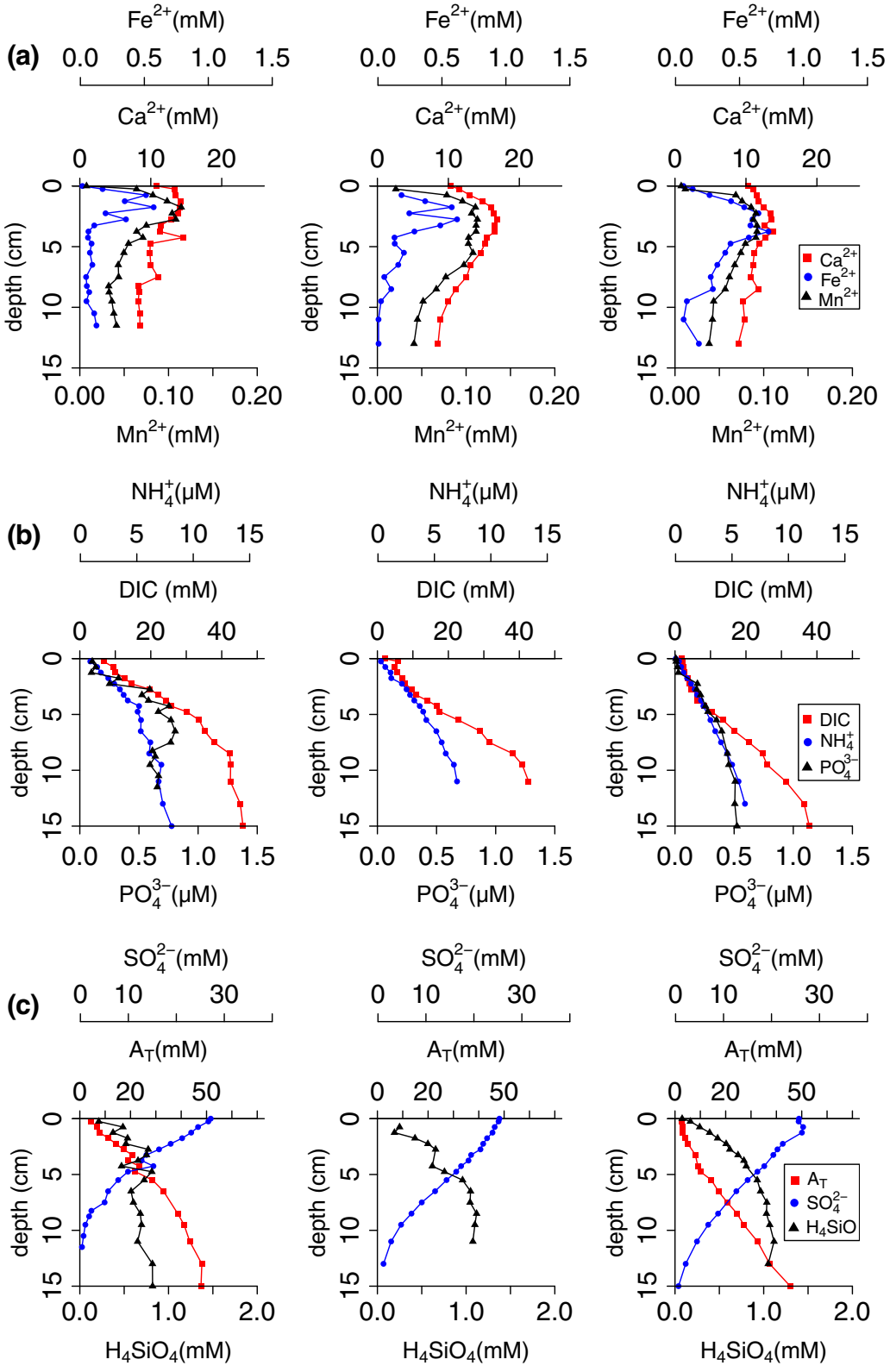

Fig. 5. Pore water depth profiles recorded at the field site in January (left column), March (middle) and May (right column) 2014. Depth profiles from one replicate core (out of 2). The profile set of the second core were very similar and are not shown. (a) Ca^{2+} (red squares), Fe^{2+} (blue circles) and Mn^{2+} (black triangles). (b) Dissolved Inorganic Carbon (DIC, red squares), NH_4^+ (blue circles) and PO_4^{3-} (black triangles). (c) Total Alkalinity (A_T, red squares), SO_4^{2-} (blue circles) and H_4SiO_4 (black triangles). Data values at 0 cm represent the bottom water concentrations, sampled at ~1 m above the sediment surface. (For interpretation of the references to colour in this figure legend, the reader is referred to the web version of this article.)

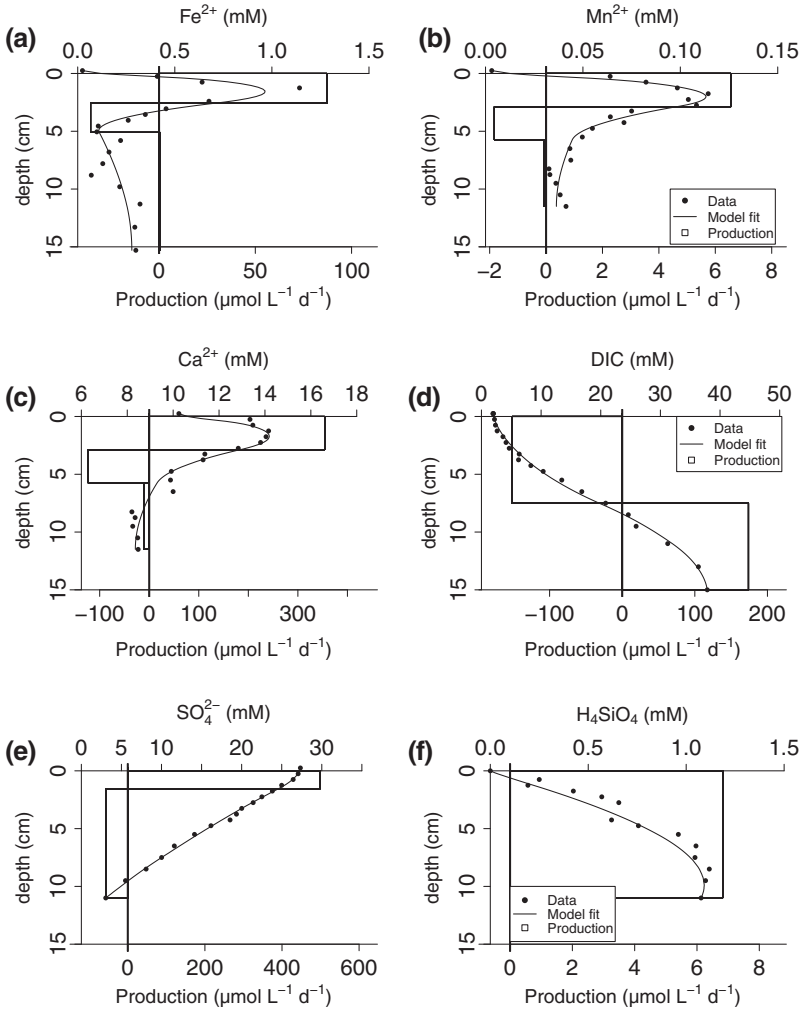

Fig. 6. Example of inverse modeling results obtained by PROFILE analysis. The graphs show the vertical depth profiles of pore water concentrations (solid circles), the model fit of the underlying diagenetic model (solid line) and the net production rate estimated by the PROFILE model fitting procedure (solid boxes). The vertical solid line represents the zero net production.

of Fe^{2+} in the top few centimeters (coinciding with the suboxic zone), which was followed by intense removal of Fe^{2+} in the next 2–3 cm just below the production zone.

The depth profiles of Mn^{2+} and Ca^{2+} (Fig. 5a) were similar, and showed an increase within the upper 4 cm, followed by a subsequent decrease in deeper layers. The maximum pore water concentration of Mn^{2+} was ~0.1 mM over the three sampling campaigns. The Ca^{2+} concentration increased from ~10 mM in the overlying water to maximum values higher than 17 mM at ~3 cm. Below 5 cm, the Ca^{2+} concentration decreased again to background values around 10 mM. PROFILE analysis (Fig. 6b and c) confirmed the concomitant production of Ca^{2+} and Mn^{2+} in the top zone and a consumption in the deeper sediment layers. All three solutes (Fe^{2+}, Ca^{2+} and Mn^{2+}) show an increased production in March as compared to January and May (Table 2), coinciding with the expansion of the suboxic zone and the extension of the acidic conditions deeper into the sediment.

The NH_4^+ and PO_4^{3-} depth profiles showed a similar buildup with depth, suggesting nutrient release during organic matter mineralization. The NH_4^+ concentration increased steadily from low values (i.e. below the detection limit) at the SWI to 6 mM in deeper layers. Similarly, PO_4^{3-} increased also from non-detectable values in the overlying water to 0.5 mM at depth, though the gradient was steeper in January compared to May. NO_3^- and NO_2^- values were below the detection limit (<0.2 μM) at all depths during the sampling period. PROFILE analysis of the NH_4^+ and PO_4^{3-} depth profiles resulted in a single production zone spanning the whole sampling depth (data not shown). The ratio of the depth integrated production rates for NH_4^+ (4.1 ± 1.4 mmol m^{-2} d^{-1}) and PO_4^{3-} (0.22 ± 0.04 mmol m^{-2} d^{-1}) was 18.6 ± 7.2, which closely approaches the Redfield N:P ratio of 16 of marine phytoplankton (Redfield, 1934).

In all three months, DIC increased from the water column value around 2.1 mM to reach high values at depth (42 mM at 10 cm in January and March and 26 mM at 10 cm in May; Fig. 5c). DIC values first increased slowly throughout the suboxic zone, and then increased more rapidly afterwards, resulting in a notable inflection of the

Table 2
Summary of the net volumetric production rates (mmol m^{-3} d^{-1}) in the (upper) electro-active zone and the deeper zone beneath the electro-active zone. Negative values indicate net consumption, positive values net production. All rate estimates are obtained from analyses of pore water depth profiles using the PROFILE software (Berg et al., 1998) corrected for ionic drift – see Appendix. Values are given as the (mean ± s.d.) calculated from depth profiles in replicate cores. DIC = Dissolved Inorganic Carbon.

		January	March	May
DIC	Upper zone	−131 ± 147	−160 ± 68	−302 ± 323
	Lower zone	312 ± 166	234 ± 56	142 ± 85
SO_4^{2-}	Upper zone	499 ± 726	244 ± 247	120 ± 100
	Lower zone	−120 ± 22	−151 ± 11	−82 ± 35
Fe^{2+}	Upper zone	61 ± 38	38.8 ± 1.3	33 ± 13
	Lower zone	−25 ± 14	−11.2 ± 1.6	−9 ± 6
Ca^{2+}	Upper zone	567 ± 301	634 ± 203	210 ± 96
	Lower zone	−115 ± 11	−73 ± 20	−21 ± 2.1
Mn^{2+}	Upper zone	5.9 ± 0.9	9 ± 3	4.4 ± 1.8
	Lower zone	−2.0 ± 0.2	−0.4 ± 0.1	−0.24 ± 0.08

depth profile at around 4–6 cm from concave up to concave down. In accordance with this, PROFILE analysis suggested a strong apparent consumption in the upper zone and a production of DIC in the lower sediment layer. Below 5 cm, the volumetric DIC production rate varied between 142 ± 85 μM d^{-1} in May to 312 ± 166 μM d^{-1} in January (Fig. 6d, rates are presented in Table 2).

In January and March, the sulfate depth profile decreased from ~26.6 ± 1.1 mM in the overlying water to non-detectable values in sediment horizon between 12 and 15 cm (Fig. 5c). In May, the SO_4^{2-} depth profile showed a subsurface maximum at ~2 cm. The sulfate depletion zone occurred slightly deeper in March and May, but such a difference could also be due to variability between cores. PROFILE analysis always indicated a net production of sulfate (~290 μM d^{-1}) in the upper few centimeters, followed by a net consumption (~120 μM d^{-1}) in deeper sediment layers (Fig. 6e, rates are presented in Table 2).

The release of silicate (Fig. 5c) due to the dissolution of biogenic silica resulted in an increase from low values in the overlying water (<0.1 μM) to an asymptotic value of ~1 mM at depth. The integrated production rate of silica was highest in March (0.81 ± 0.08 mmol m^{-2} d^{-1}) and lowest in January (0.45 ± 0.27 mmol m^{-2} d^{-1}).

The pore water alkalinity (A_T) gradually increased to reach values of ~50 mM at 15 cm depth in both January and May (Fig. 5c). No pore water alkalinity data were obtained in March. The concentration depth profile of A_T showed three zones: a relatively sharp increase in the upper 5 mm (indicative of strong production near the SWI), followed by a concave up profile in the suboxic zone (indicating consumption of alkalinity), to become concave down towards depth (suggesting again the production of alkalinity). This concave down shape was not obvious in March. The strong gradients in the A_T profile near the interface could not be resolved by PROFILE analysis (not enough data points), therefore the rates predicted by PROFILE were not included in the further analysis.

3.6. Cathodic O_2 consumption and current density

The current density generated by electrogenic sulfur oxidation was calculated in two different ways from the alkalinity depth profile (Table 1). The current density calculated within the oxic zone (cathodic oxygen reduction) provided similar values as the current density calculated in the suboxic zone (anodic sulfide reduction). This shows that the two redox half-reactions balance each other out in terms of electrons, and thus that the principle of charge conservation is kept. The final current density value was calculated as the average of both values, and was comparable in January (29.4 ± 3.3 mA m^{-2}) and May (26 ± 19 mA m^{-2}). This current density corresponds with a mean electrical field of E = 14.4 ± 2.3 mV m^{-1} (Table 1). This value is ~6 times lower than the range 80–100 mV m^{-1} recorded by Risgaard-Petersen et al. (2012) in a recent laboratory sediment incubation.

DOU values (Table 1) were slightly lower (13.2 ± 4.0 mmol m^{-2} d^{-1}) in January than in May (16.8 ± 5.5 mmol m^{-2} d^{-1}), but were not significantly different. The percentage of the DOU (p) consumed by cathodic oxygen reduction (Eq. (4); Fig. 1d) declines from January (50 ± 16%) to May (34 ± 28%). No estimates for p and the current density J are available in March as pore water alkalinity data were lacking, but in further calculations, we assumed that the current density in March is the average of January and May. From these current densities, and assuming that free sulfide is fully oxidized to sulfate (i.e. releasing 8 electrons), we can calculate the reaction rate of anodic sulfide oxidation as 3.29 ± 0.36 mmol S m^{-2} d^{-1} in January and 2.9 ± 2.2 mmol S m^{-2} d^{-1} in May.

4. DISCUSSION

Electro-active sediments have only been recently discovered (Nielsen et al., 2010) and distinguish themselves from other sedimentary environments by the presence of electrical currents in the surface layer of the sediment. The underlying electron transport is induced by metabolic activity of long filamentous cable bacteria (Pfeffer et al., 2012), in a process referred to as electrogenic sulfur oxidation (Malkin et al., 2014). We document here the metabolic activity of cable bacteria under *in situ* conditions by describing their geochemical signature, biomass density and the generated electrical field. We continue by estimating the mineralization rate of organic matter at the field site

and showing that cable bacteria strongly modulate the sedimentary biogeochemical cycling. We conclude by presenting a budget of the geochemical cycling at the field site.

4.1. The geochemical signature of e-SOx

Electrogenic sulfur oxidation induces a characteristic geochemical signature in the pore water (Nielsen et al., 2010; Meysman et al., 2015), which consists of: (i) a shallow oxygen penetration and a high diffusive oxygen uptake, (ii) H_2S and O_2 that are separated by a several millimeter thick suboxic zone, where neither compounds are present in detectable concentrations, and (iii) the pH depth profile shows strong excursions, with a alkaline maximum near the surface and an acidic minimum near the end of the suboxic zone. Microsensor profiling of O_2, H_2S and pH (Fig. 3) showed that this geochemical fingerprint was present from January throughout May 2014, suggesting that e-SOx was the dominant sulfur oxidation pathway at the field site during this period.

Our results show a clear correlation between the depth distribution of the cable bacteria and the width of the suboxic zone, providing further evidence that the metabolic activity of the cable bacteria is generating the observed e-SOx geochemical fingerprint. The width of the suboxic zone can be calculated by subtracting the Oxygen Penetration Depth (OPD, last detectable oxygen) from the Sulfide Appearance Depth (SAD, first detectable free sulfide). The SAD of 5.0 ± 1.4 cm in March leads to a suboxic zone of 4.8 cm, which is much deeper than was previously observed in both field surveys (1.2–1.6 cm in Malkin et al., 2014) and laboratory experiments (0.7–2.5 cm; Nielsen et al., 2010; Pfeffer et al., 2012; Risgaard-Petersen et al., 2012, 2014; Damgaard et al., 2014; Schauer et al., 2014; Vasquez-Cardenas et al., 2015). The filament density profile confirms that cable bacteria were present up to 7 cm deep in March and this largely extends the range of 0.8–3.2 mm previously recorded in laboratory experiments (Nielsen et al., 2010; Pfeffer et al., 2012; Risgaard-Petersen et al., 2012, 2014; Marzocchi et al., 2014; Schauer et al., 2014; Larsen et al., 2015; Malkin and Meysman, 2015; Vasquez-Cardenas et al., 2015). If the observed cable bacteria in these deep layers are metabolically active, this implies that they must have an electrical connection to the oxic zone, suggesting that microbial mediated long-distance transport can bridge far longer distances than previously thought.

Cable bacteria in electro-active sediments can be responsible for the major part of the oxygen consumption (Nielsen et al., 2010; Risgaard-Petersen et al., 2014). Previous estimates of the contribution p of cable bacteria to the total oxygen uptake ranged from 25% to 82% in laboratory incubations and 5–34% in the field (Nielsen and Risgaard-Petersen, 2015). The model study by Meysman et al. (2015) reported that 93% of the DOU was consumed by cathodic oxygen reduction. Here, we obtained an average DOU of 14.8 ± 1.8 mmol m^{-2} d^{-1} over the sampling period with $42 \pm 11\%$ of DOU consumed by cable bacteria. Malkin et al. (2014) determined the DOU and the value of p at the same field station, and reported higher values for the DOU (32 ± 15 mmol m^{-2} d^{-1} in October 2011 and 25 ± 21 mmol m^{-2} d^{-1} in March 2013) and lower values for p ($19.1 \pm 7.1\%$ in October 2011 and $5.3 \pm 2.9\%$ in March 2013). These differences in DOU values may be explained by either seasonality (the high value of 32 mmol m^{-2} d^{-1} was measured in October and not in spring) and/or strong lateral heterogeneity in the O_2 consumption of the sediment, as suggested by the relative large standard deviation on the DOU recorded by Malkin et al. (2014).

The pH depth profile showed strong excursions, with the pH minimum ranging from 6.35 ± 0.25 in January to 6.54 ± 0.14 in March, and a similar acidification of the suboxic zone was also found by Malkin et al. (2014) at the same site. The observation of strong proton consumption near the OPD and proton production near the SAD fully fits the current conceptual model of proton cycling induced by electrogenic sulfur oxidation (Nielsen et al., 2010; Meysman et al., 2015; Fig. 1d). It should be noted however that the typical subsurface pH maximum near the OPD was only observed in January. In the other two months, this pH peak was not recorded, but the pH depth profile still shows a notable change in the gradient near the OPD (thus still indicating proton consumption). Our results hence indicate that the subsurface pH maximum is not as characteristic for the e-SOx fingerprint as previously thought (Meysman et al., 2015). The absence of the subsurface pH maximum can be explained by a closer examination of the local transport and production of alkalinity near the sediment–water interface. As the oxygen penetration depth is very small, cathodic oxygen reduction (COR) must take place within in a very narrow oxic zone, together with the strong alkalinity release associated with COR occurs very close to the SWI (Rao et al., 2016). Accordingly, the alkalinity released is rapidly lost to the overlying water by diffusion, which hence diminishes the magnitude of the pH maximum. The alkalinity consumption associated with anodic sulfide oxidation occurs over a much deeper and wider zone, and hence, the pH minimum at depth is less sensitive to diffusive smoothening. The fact that the pH drops to low values (below 7) within the suboxic zone appears to be a more robust geochemical proxy for the presence of e-SOx, than the presence of a shallow subsurface pH peak.

4.2. Cable bacteria densities and current density

In laboratory incubation experiments, in which cable bacteria are enriched in homogenized sediment, high current densities have been obtained: 95 mA m^{-2} (Schauer et al., 2014), 232 mA m^{-2} (Vasquez-Cardenas et al., 2015), and 381 mA m^{-2} (Risgaard-Petersen et al., 2014). The current densities that we observed under field conditions at Station 130 are one order of magnitude lower (25–32 mA m^{-2}), indicating that electrogenic sulfur oxidation under field conditions occurs at a lower rate compared to idealized laboratory conditions. The current densities recorded here are however fully in line with those obtained by Malkin et al. (2014) at the same site in October 2011 (25.2 ± 2.6 mA m^{-2}), though higher than the values reported in March 2013 (4.6 ± 1.8 mA m^{-2}). This latter dif-

ference could be due to inter-annual variation in the rate of e-SOx, but could also be due to the different way in which the current density was estimated (see Section 3.6), i.e., directly from the alkalinity profile as is done here, or indirectly from the pH depth profile as in Malkin et al. (2014).

The volumetric densities of cable bacteria of 20–100 m cm^{-3} that we recorded within the suboxic zone closely agree with those previously observed at the field site (123 m cm^{-3}) as well as those at another coastal site in the North Sea area (82 m cm^{-3}) as reported by Malkin et al. (2014). Our volumetric densities also correspond to the range 127–147 m cm^{-3} observed in some laboratory incubations (Pfeffer et al., 2012; Larsen et al., 2015), although other laboratory experiments record higher values (50–1600 m cm^{-3}; Schauer et al., 2014; Vasquez-Cardenas et al., 2015). No other field observations of depth profiles of cable bacteria filament densities have been previously reported.

The integrated filament densities obtained here (168–352 m cm^{-2}) are the first field values reported, and are about 6 times lower than those observed in laboratory experiments (1100–2400 m cm^{-2}; Schauer et al., 2014; Vasquez-Cardenas et al., 2015). The comparison between laboratory experiments and field observations (Fig. 7) shows that the filament density (cable bacteria abundance) systematically increases with the recorded current density (cable bacteria metabolic activity). This linear relation (the cable bacteria density increases with 14 m cm^{-2} for every 1 mA m^{-2} increase of the current density) suggests a mechanism in which cable bacteria population size is electron donor controlled. A higher electron donor supply induces a higher current density, and the resulting free energy liberated by electrogenic sulfur oxidation allows a larger population density of cable bacteria to be sustained.

4.3. Electrical field and ionic drift

The electron current generated by cable bacteria creates an electrical field, which will drive an ionic counter-current in the pore water (Risgaard-Petersen et al., 2012). This phenomenon is easily explained in terms of charge balance. Cable bacteria harvest electrons from the pore water via anodic sulfide oxidation and transport those electrons along their filaments to the SWI, where cathodic oxygen reduction again removes these electrons. This spatial segregation of the two redox half reactions creates a charge imbalance in the sediment (positive charges accumulate at depth, negative charge near the SWI). This charge accumulation in its turn creates an electrical field, which will drive an ionic drift in the pore water (Risgaard-Petersen et al., 2012). In this ionic drift, negative ions will be forced to migrate downwards, and conversely, positive ions will move upwards. Recently, Risgaard-Petersen et al. (2014) used a novel electrical potential micro-electrode to measure the build-up in electrical potential associated with the electrical field (Damgaard et al., 2014).

Our calculations indicate that ionic drift can have a significant impact on the transport of ions in electro-active sediments, and should be taken into account when estimating fluxes and production (Risgaard-Petersen et al., 2014; Rao et al., 2016). As predicted by the Nernst-Planck expression $I = -\varphi D_s zFEC/(RT)$, ions with multiple charges (large z) that are also abundant in the pore water (large C) are more strongly influenced by ionic drift. In the case of Ca^{2+}, ionic drift was responsible for ~30% of the total efflux across the SWI in January and May, and so Ca^{2+} shows much less accumulation in the pore water than without ionic drift. For negatively charged species, the ionic drift is counteracting the (negative) flux out of the sediment by adding a positive flux component (drawing anions into the sediment). This is most pronounced for SO_4^{2-}, where the ionic drift term leads to a net influx that was ~75% higher. Accordingly, sulfate shows a more pronounced accumulation in the top layer of the sediment than without ionic drift. The effect of ionic drift for all ions is summarized in Table 3.

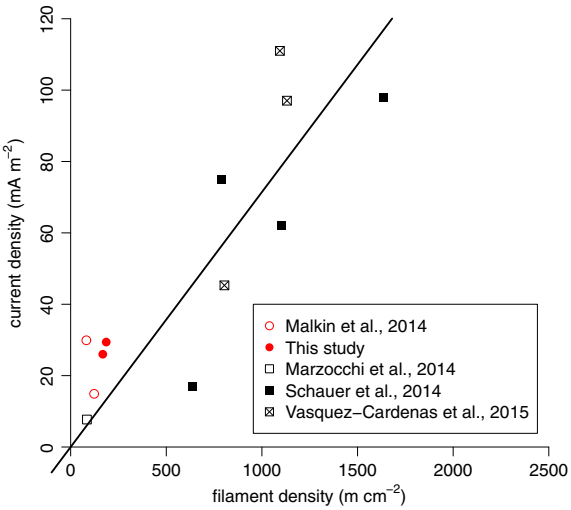

Fig. 7. Relation between the current density (mA m^{-2}) generated by electrogenic sulfur oxidation and the filament density of cable bacteria obtained by FISH (m cm^{-2}). Circles represent field data, squares represent laboratory sediment incubation experiments. Data are based on the results here and previous publications. The solid line shows the linear regression line. Note that the filament density obtained by Schauer et al. (2014) was obtained by a different counting procedure as the other datasets (the values from this publication are normalized to be comparable with the other data).

4.4. Organic matter mineralization

The mineralization of organic matter and nutrients is the dominant driving force of early diagenetic transformations in marine sediments (Burdige, 2006; Aller, 2014). Through sulfate reduction, mineralization also supplies the reduced sulfide (either as free sulfide or metal sulfides; see below) that serves as the electron donor in electrogenic sulfur oxidation. We determined the mineralization rate at the field site in three different ways, based on the depth profiles of three different geochemical markers: DIC, NH_4^+ and SO_4^{2-}. We now discuss each approach separately.

Two major processes contribute to the production rate of DIC (P_{DIC}) in a typical marine sediment: organic matter mineralization (R_{min}) and $CaCO_3$ dissolution (R_{CaCO_3})

Table 3
Summary of calculated ionic drift terms and solute fluxes. Diffusive fluxes across the SWI ($J_{diff,up}$) and bottom boundary ($J_{diff,down}$) were estimated by PROFILE analysis (Berg et al., 1998) of pore water depth profiles. NA values had a zero flux imposed as boundary condition in PROFILE. Ionic drift terms at the SWI (I_{SWI}) and at the sulfide appearance depth (I_{SAD}) were calculated as explained in the Appendix. Values represent (mean ± 1 s.d.) of depth profiles in replicate cores. Negative values are oriented upwards, positive values are directed downwards into the sediment. (*) DIC was influenced by a sampling artefact in the top zone (as described in Section 4.4), so no reliable flux could be estimated.

Parameter		Units	January	March	May
Fe^{2+}	I_{SWI}	mmol m^{-2} d^{-1}	−0.08 ± 0.05	−0.006	−0.02 ± 0.01
	I_{SAD}	mmol m^{-2} d^{-1}	−0.12 ± 0.09	−0.02 ± 0.02	−0.2 ± 0.04
	$J_{diff,up}$	mmol m^{-2} d^{-1}	−1.0 ± 0.6	−0.8 ± 0.2	−0.9 ± 0.2
	$J_{diff,down}$	mmol m^{-2} d^{-1}	NA	NA	NA
Mn^{2+}	I_{SWI}	mmol m^{-2} d^{-1}	−0.021 ± 0.004	−0.007 ± 0.003	−0.006 ± 0.004
	I_{SAD}	mmol m^{-2} d^{-1}	−0.04 ± 0.01	−0.019 ± 0.003	−0.024 ± 0.002
	$J_{diff,up}$	mmol m^{-2} d^{-1}	−0.130 ± 0.002	−0.22 ± 0.04	−0.13 ± 0.03
	$J_{diff,down}$	mmol m^{-2} d^{-1}	NA	NA	NA
Ca^{2+}	I_{SWI}	mmol m^{-2} d^{-1}	−5 ± 1	−3.0 ± 0.3	−3.1 ± 0.1
	I_{SAD}	mmol m^{-2} d^{-1}	−4.7 ± 0.6	−3.5 ± 0.2	−4.3 ± 0.9
	$J_{diff,up}$	mmol m^{-2} d^{-1}	−9.0 ± 4.1	−15.2 ± 2.3	−6.1 ± 2.4
	$J_{diff,down}$	mmol m^{-2} d^{-1}	NA	NA	NA
SO_4^{2-}	I_{SWI}	mmol m^{-2} d^{-1}	10.6 ± 0.6	8.2 ± 0.1	9.36 ± 0.02
	I_{SAD}	mmol m^{-2} d^{-1}	8.0 ± 0.2	5.2 ± 0.1	8.0 ± 0.2
	$J_{diff,up}$	mmol m^{-2} d^{-1}	3.6 ± 8.6	2.3 ± 5.0	3.6 ± 2.0
	$J_{diff,down}$	mmol m^{-2} d^{-1}	−1.5 ± 0.8	1.7 ± 1.0	3.0 ± 4.3
DIC (*)	I_{SWI}	mmol m^{-2} d^{-1}	1.2 ± 0.4	0.9 ± 0.1	0.7 ± 0.3
	I_{SAD}	mmol m^{-2} d^{-1}	3.1 ± 0.5	3.06 ± 0.01	1.3 ± 0.4
	$J_{diff,up}$	mmol m^{-2} d^{-1}	NA	NA	NA
	$J_{diff,down}$	mmol m^{-2} d^{-1}	2.3 ± 3.9	−3.40 ± 0.09	−2.3 ± 5.0
NH_4^+	I_{SWI}	mmol m^{-2} d^{-1}	−0.30 ± 0.07	−0.08	−0.07 ± 0.04
	I_{SAD}	mmol m^{-2} d^{-1}	−1.1 ± 0.1	−1.20 ± 0.04	−0.48 ± 0.01
	$J_{diff,up}$	mmol m^{-2} d^{-1}	−4.6 ± 0.8	−5.7 ± 0.5	−4.0 ± 0.1
	$J_{diff,down}$	mmol m^{-2} d^{-1}	−0.5 ± 0.6	−1.7 ± 0.5	−1.4 ± 0.1
PO_4^{3-}	I_{SWI}	mmol m^{-2} d^{-1}	0.02 ± 0.01	NA	0.002 ± 0.001
	I_{SAD}	mmol m^{-2} d^{-1}	0.07 ± 0.02	NA	0.036 ± 0.004
	$J_{diff,up}$	mmol m^{-2} d^{-1}	−0.22 ± 0.03	NA	−0.161 ± 0.006
	$J_{diff,down}$	mmol m^{-2} d^{-1}	NA	NA	−0.009 ± 0.004
H_4SiO_4	I_{SWI}	mmol m^{-2} d^{-1}	Not charged	Not charged	Not charged
	I_{SAD}	mmol m^{-2} d^{-1}	Not charged	Not charged	Not charged
	$J_{diff,up}$	mmol m^{-2} d^{-1}	0.02 ± 0.18	−0.12 ± 0.07	−0.12 ± 0.02
	$J_{diff,down}$	mmol m^{-2} d^{-1}	0.47 ± 0.02	0.68 ± 0.01	0.5 ± 0.9

$$P_{DIC} = R_{min} + R_{CaCO_3} \quad (2)$$

The DIC production rate P_{DIC} was calculated from PROFILE analysis of DIC depth profiles. Similarly, the rate of carbonate dissolution R_{CaCO_3} can be obtained from PROFILE analysis of the Ca^{2+} depth profile (see Section 3.5). When this rate is corrected for ionic drift (see previous section), this leads to an estimated carbonate dissolution rate of $R_{CaCO_3} = 13.9 \pm 7.9$ mmol m^{-2} d^{-1} within the suboxic zone. This way, the mineralization rate R_{min} is the only unknown remaining in Eq. (2) and can be calculated. However, one challenge with this approach is that the DIC depth profile showed a clear signature of DIC consumption in the suboxic zone (which is not accounted for in Eq. (2)). PROFILE analysis estimated that the DIC consumption rate over the first 3–5 cm was −5.9 ± 2.7 mmol m^{-2} d^{-1} (average over 3 months). There are four possible explanations for this DIC consumption: (i) carbonate precipitation, (ii) ionic drift, (iii) chemoautotrophy, and (iv) a sampling artefact. We now evaluate each option separately. First, the precipitation of high Mg carbonates has been observed in e-SOx incubations under laboratory conditions (Risgaard-Petersen et al., 2012). However the precipitation occurs right at the SWI, and not in the suboxic zone where the DIC consumption takes place. Thus we can rule out carbonate precipitation as an explanation for the observed DIC consumption. Second, ionic drift will influence the transport of bicarbonate ions (see Section 4.2). When calculating the ionic drift effect on the HCO_3^- production, this leads to an apparent consumption of 1.5 ± 0.8 mmol m^{-2} d^{-1} within the suboxic zone (the ionic drift effect is positive for negatively charged ions, however, the net effect of ionic drift on the suboxic zone is dependent on the concentrations at the boundaries

of the zone, and can lead to a net negative effect, see Eq. (A.8) in Appendix A). Accordingly, ionic drift has the opposite effect on DIC (production instead of consumption) and increases the effective DIC consumption to ~4.3 mmol m^{-2} d^{-1}. Third, Vasquez-Cardenas et al. (2015) has recently shown in laboratory incubations that cable bacteria and the associated microbial community can induce chemo-autotrophy rates up to ~11 mmol C m^{-2} d^{-1} (depth integrated rate in the upper 3 cm). As the filament density and current density in the laboratory experiment of Vasquez-Cardenas et al. (2015) were ~4 times higher than here, and assuming that the chemo-autotrophy rate simply scales with current density, one hence expects a DIC consumption of ~2.5 mmol C m^{-2} d^{-1} due to chemo-autotrophy (thus leaving 1.8 mmol C m^{-2} d^{-1} of the DIC consumption unexplained). Fourth, the apparent DIC consumption could be a sampling artefact due to the acidic pH of the suboxic zone. During pore water extraction by centrifugation, the samples were exposed to a nitrogen atmosphere, in which CO_2 can start degassing to the overlying gas phase. Since the zone of DIC consumption strongly coincides with the extent of the acidic suboxic zone, we believe that the remaining unexplained DIC consumption could be an artefact of the pore water extraction procedure.

Accordingly, we restricted our DIC analysis to the deeper zone of the sediment (>5 cm) that is not affected by acidic pH conditions. Within this zone, PROFILE analysis (Fig. 6d) showed that DIC production took place at a rate of 229 ± 85 mmol m^{-3} d^{-1}, which is the combined effect of organic matter remineralization (R_{min}) and $CaCO_3$ precipitation (negative R_{CaCO_3}). The precipitation rate of carbonates was similarly estimated from the Ca^{2+} profile (see Section 3.5) as $R_{CaCO_3} = -70 \pm 47$ mmol m^{-3} d^{-1}. By applying Eq. (2), the volumetric mineralization rate hence becomes 299 ± 97 mmol m^{-3} d^{-1}, and assuming that organic matter mineralization does not vary substantially with depth, this hence provides an integrated mineralization rate of 45 ± 14 mmol m^{-2} d^{-1} over the whole sediment column (0–15 cm).

A second way to estimate the mineralization rate is through the production rate of NH_4^+. If we assume that all nitrogen is released by mineralization as NH_4^+, we can estimate the mineralization rate as

$$R_{min} = \frac{C}{N} \cdot (P_{NH_4^+} - I_{NH_4^+}) \quad (3)$$

with C/N is the carbon to nitrogen stoichiometry of organic matter (8.54 ± 0.85; see Section 3.4), $P_{NH_4^+}$ is the integrated production rate of ammonium over the sediment as estimated by PROFILE analysis (4.1 ± 1.4 mmol m^{-2} d^{-1}), and $I_{NH_4^+}$ is the net ionic drift effect on ammonium. Together, this provides an integrated mineralization rate of 36 ± 10 mmol m^{-2} d^{-1}, which is comparable to the estimate obtained from DIC analysis.

A third way to estimate the mineralization rate is via the sulfate reduction rate (SRR), calculated from the sulfate profiles. Although the rates were not quantified, we believe that there is a negligible reduction of iron and manganese oxides at the field site, due to the absence of physical reworking of the sediment, which is crucial to sustain any metal cycling in the sediment (Canfield et al., 1993). Combined with the shallow oxygen penetration depth (limiting aerobic respiration) as well the low NO_3^- concentrations (limiting nitrate respiration), this suggests that organic matter was almost exclusively oxidized by sulfate reduction. Under this condition, the mineralization rate can be calculated from the sulfate production rate as,

$$R_{min} = -2.(P_{SO_4^{2-}} - I_{SO_4^{2-}}) \quad (4)$$

with $P_{SO_4^{2-}}$ the consumption rate of sulfate, which can be calculated as explained above.

The top layer of the sediment showed a net production of sulfate, likely linked to the oxidation of sulfide by e-SOx. To correct for this effect, the net sulfate consumption was estimated in the bottom part by PROFILE analysis (118 ± 35 mmol m^{-3} d^{-1}; no correction needed for ionic drift as the electrical field vanishes in deeper layers) and subsequently integrated over the whole depth domain, assuming that the sulfate reduction rate is constant with depth. Together, this provides an estimate of mineralization rate $R_{min} = 35 \pm 10$ mmol C m^{-2} d^{-1}, which is comparable to the previously results from DIC and NH_4^+ analysis. The values are in close agreement for all months. Therefore an average monthly mineralization rate obtained from the three different estimates (39 mmol C m^{-2} d^{-1}) was used in further calculations.

The mineralization rates obtained here are in the range of the expected ones for coastal sediments with shallow water depth (Thamdrup et al., 1994; Burdige, 2006). Net primary production in the Southern Bight of the North-Sea is 46–70 mmol C m^{-2} d^{-1} (van Beusekom and Diel-Christiansen, 1994; Lancelot et al., 2005), of which 20% (7–14 mmol C m^{-2} d^{-1}) has been estimated to end up in the sediment. The mineralization rate in the sediment estimated here is however substantially higher, indicating that the sediment column is responsible for a much larger part (~56–85%) of the total remineralization. The specific location of the field site (close to shore, shallow water column of 10 m) may explain this strong benthic-pelagic coupling.

4.5. Biogenic silica dissolution e-SOx

Diatoms are the main producers of biogenic silica ($bSiO_2$) in the coastal ocean. A major fraction of the $bSiO_2$ produced is recycled by dissolution in the water column, while the remaining part reaches the sediment where it dissolves to form dissolved silicate (H_4SiO_4). To estimate the effect of e-SOx on the dissolution of biogenic silica, we can estimate the expected dissolution rate and compare it to the measured dissolution rate, based on the porewater profiles. Using PROFILE, we calculated the dissolution rate of biogenic silica ($bSiO_2$) from the H_4SiO_4 depth profile. The equilibrium concentration of H_4SiO_4 ~1 mM (Fig. 5c) and estimated dissolution rates R_{bSi} varied between 0.45 ± 0.27 mmol Si m^{-2} d^{-1} in January and 0.81 ± 0.08 mmol Si m^{-2} d^{-1} in March (Table 1). Lancelot et al. (2005) estimated that 15% of the organic matter input to the BCZ to the sediment consists of diatoms. The average Si:C ratio of marine diatoms is 0.12

(Brzezinski, 1985) and if the dissolution of biogenic silica matches the input to the sediment then on average ~0.70 mmol Si m^{-2} d^{-1} should be released. This is consistent with the dissolution rates estimated here. The recorded dissolution rates and equilibrium values show great variability under natural sedimentary conditions, and the environmental controls remain poorly known (Dixit et al., 2001).

4.6. Iron and sulfur cycling

The e-SOx metabolism of cable bacteria relies on a supply of suitable electron donors, although it has been suggested that reduced organic carbon compounds could be involved (Risgaard-Petersen et al., 2012). Yet until now, only sulfide has been unequivocally demonstrated to act as an electron donor (anodic sulfide oxidation as in Eq. (B.1); Fig. 1d). Although no free sulfide is detectable in the suboxic zone, cable bacteria have a high affinity for sulfide, which thus still allows strong sulfide consumption by e-SOx within the suboxic zone, giving rise to cryptic sulfur cycling (Meysman et al., 2015). The sulfide that is consumed by e-SOx within the suboxic zone can originate from three distinct sources; (i) free sulfide diffusing upwards from the deeper anoxic zone, which is produced by sulfate reduction in deeper horizons (ii) free sulfide liberated from local FeS dissolution, and (iii) free sulfide produced by local sulfate reduction (Risgaard-Petersen et al., 2012).

The sulfide flux from the deeper sediment to the upper zone was estimated from the gradient of the $\sum H_2S$ profiles (~300 mmol m^{-4}), multiplied by the effective diffusion coefficient (1.15 10^{-4} m^2 d^{-1}) and the porosity (0.78), which provides a low flux of 0.03 mmol m^{-2} d^{-1}. The upward flux of sulfide is hence negligible as a sulfide source for e-SOx. The second source of sulfide is the dissolution of iron sulfides. The associated dissolution rate can be estimated from the inventory change of AVS in the top 2.5 cm (217 ± 174 mmol S per m^2 sediment over 117 days; Fig. 4c), thus resulting in $R_{FeS} = 1.9 \pm 1.5$ mmol m^{-2} d^{-1}. Alternatively, R_{FeS} can also be estimated from the production rate of Fe^{2+}, which was estimated as 1.3 ± 1.0 mmol m^{-2} d^{-1} by PROFILE analysis (Fig. 6a) and became 1.2 ± 1.0 mmol m^{-2} d^{-1} after the correction for ionic drift. A third source of sulfide is mineralization coupled to sulfate reduction. The sulfate reduction rate (SRR) for the whole sediment column was already estimated in Section 4.4. We can rescale this SRR to the upper 3 cm (the suboxic zone affected by e-SOx), which leads to a SRR of 3.7 ± 1.5 mmol S m^{-2} d^{-1}. If we assume that the free sulfide in the suboxic zone resides in a steady state, then the sum of the production via FeS dissolution (1.2 mmol m^{-2} d^{-1}), the flux from below (0.03 mmol m^{-2} d^{-1}) and production via sulfate reduction must match the sulfide consumption via e-SOx (3.3 mmol m^{-2} d^{-1}), thus implying an SRR of 2.1 mmol S m^{-2} d^{-1} throughout the suboxic zone, which means we most likely overestimated the SRR in the suboxic zone. The sulfide that results from sulfate reduction will be re-oxidized to sulfate and immediately reduced again, leading to a zero net effect on sulfate. On the other hand, oxidation of sulfide that is released by FeS dissolution results in net accumulation of 1.2 mmol S m^{-2} d^{-1} over the suboxic zone, which falls within the uncertainty range of the PROFILE estimate corrected for ionic drift (0.7 ± 2.3 mmol S m^{-2} d^{-1}). Adopting this revised SRR (2.1 mmol S m^{-2} d^{-1}), sulfate reduction provides 63% of the free sulfide for e-SOx in our sediment, while FeS dissolution provides the remaining 37% and the flux from below is insignificant (<1%). This contribution of FeS dissolution is much lower than previously observed in laboratory experiments, where iron sulfide dissolution has been the dominant source, providing up to 88% of the free sulfide for e-SOx (Risgaard-Petersen et al., 2012). As laboratory experiments typically start from homogenized sediment mixtures and this creates an artificially high iron sulfide pool, which could explain the difference between laboratory and field estimates. This idea is supported by recent biogeochemical model simulations of sulfur cycling in natural electro-active sediments, which predict a contribution of only 40% from iron sulfide dissolution (Meysman et al., 2015) and this is in line with our estimate here.

A characteristic feature of electro-active sediments is a high accumulation of ferrous iron within the pore water (Risgaard-Petersen et al., 2014; Rao et al., 2016). As the total Fe^{2+} release to the pore water (1.2 mmol m^{-2} d^{-1}; PROFILE estimate corrected for ionic drift) is similar to estimated rate of FeS dissolution (1.9 mmol m^{-2} d^{-1}), this indicates that dissimilatory iron oxide reduction is likely negligible in sediment (as discussed above in Section 4.4). The Fe^{2+} released by FeS dissolution diffuses to the SWI, where it is either oxidized as iron (hydro)oxides or released into the overlying water, or alternatively, diffuses downwards into the anoxic zone, and re-precipitates as FeS. Our results show that ~1/3 of the Fe^{2+} released in the upper zone diffuses downwards and precipitates as FeS (rates vary from 0.34 ± 0.02 mmol m^{-2} d^{-1} in March to 0.6 ± 0.3 mmol m^{-2} d^{-1} in May). Accordingly, the major part of the Fe^{2+} diffuses towards the SWI, providing a flux of 0.9 ± 0.1 mmol m^{-2} d^{-1} (corrected for ionic drift, Table 3). This benthic iron flux is very high compared to the previous reports in coastal areas, which are in the range of 0.006–0.46 mmol m^{-2} d^{-1} (Wijsman et al., 2001; Severmann et al., 2010). However, caution is needed to interpret this as a net flux towards the water column, as part of Fe^{2+} can be re-oxidized to FeOOH within the oxic zone. However, as the oxic zone is small (~2.1 mm), there is not enough data resolution for PROFILE to reliably estimate the associated Fe^{2+} consumption rate. Yet, because the oxygen penetration depth is small, Fe^{2+} only requires a short diffusion time (~81 min) to migrate through the oxic zone, which increases the chance of escaping re-oxidation and being transferred to the water column. Recently, there has been considerable interest in the question of how coastal sediments can be an iron source to the ocean (Severmann et al., 2010). Accordingly, cable bacteria potentially present a new mechanism to generate a large flux of ferrous iron out of sediments, as strong iron sulfide dissolution is induced closely to the sediment–water interface.

A conspicuous observation is the enrichment of elemental sulfur in the upper zone of the sediment (Fig. 4c), which

suggests that this is somehow linked to e-SOx. Recently, Vasquez-Cardenas et al. (2015) found high rates of chemo-autotrophy associated with e-SOx in similar type of sediment, while they obtained strong indications that the metabolism of cable bacteria is based on chemo–heterotrophy. To explain their data, Vasquez-Cardenas et al. (2015) have speculated that sulfide oxidation by cable bacteria might be incomplete, and could produce partly oxidized sulfur intermediates, leading to the accumulation of S^0 in the upper 3–5 cm in our sediment column. Vasquez-Cardenas et al. (2015) claimed that the resulting S^0 pool could be used by chemo-autotrophic epsilon and gamma-proteobacteria. Elemental sulfur is a metastable sulfur phase and can disproportionate into SO_4^{2-} and HS^- through the action of sulfur disproportionating microbes (Thamdrup et al., 1993; Finster et al., 1998).

$$S^0 + H_2O \rightarrow \frac{3}{4}HS^- + \frac{1}{4}SO_4^{2-} + \frac{5}{4}H^+ \quad (5)$$

An assessment of the inventory change (similar as was done for AVS) shows a large net consumption rate of elemental sulfur of 7 ± 2 mmol S m^{-2} d^{-1} over the sampling period. Intriguingly, Rao et al. (2016) witnessed a similar depletion of S^0 in the suboxic zone in laboratory incubation experiments in which e-SOx was induced. This indicates that the observed accumulation and consumption of S^0 could be indeed linked to the presence of cable bacteria and their associated microbial communities. However, more targeted process studies (e.g. using stable S isotopes) are needed to properly elucidate the linkage between the strong S^0 cycling and cable bacteria metabolism.

4.7. Calcium and manganese cycling

In previous laboratory incubations, it was found that e-SOx strongly promotes the acidic dissolution of carbonate minerals within the suboxic zone due to the lower pH (Risgaard-Petersen et al., 2012; Rao et al., 2016). Rao et al. (2016) observed a strong increase in the carbonate dissolution alongside the development of cable bacteria in laboratory sediment incubations, which eventually led to a doubling of the DIC efflux from the sediment. Rao et al. (2016) also suggested that the accumulation of Mn^{2+} in the pore water is most likely linked to the dissolution of calcium carbonates. In this model, both Ca^{2+} and Mn^{2+} are synchronously released in the suboxic zone by carbonate dissolution. Part of the released Ca^{2+} and Mn^{2+} will diffuse towards the SWI, where they can form a magnesium rich $CaCO_3$ layer in the oxic zone (Risgaard-Petersen et al., 2012), or escape into the water column. Another part will diffuse towards the deeper sediment layers, were calcite can re-precipitate (Rao et al., 2016). When Mn^{2+} diffuses upwards, it can be oxidized to Mn^{4+} and form a manganese oxide layer or it can adsorb or co-precipitate onto calcite surfaces or the authigenic $CaMnCO_3$ phase Kutnohorite can be formed, if pore water concentrations exceed saturation (Rao et al., 2016).

Our results agree with the idea that the cycling of Ca^{2+} and Mn^{2+} are tightly linked. Foremost, PROFILE analysis indicates that the production zones of these two cations are highly similar (Fig. 6b and c). If we calculate the Ca/Mn ratio of the estimated production rates of Ca^{2+} and Mn^{2+} in the suboxic zone (which range from 48 to 101), this ratio

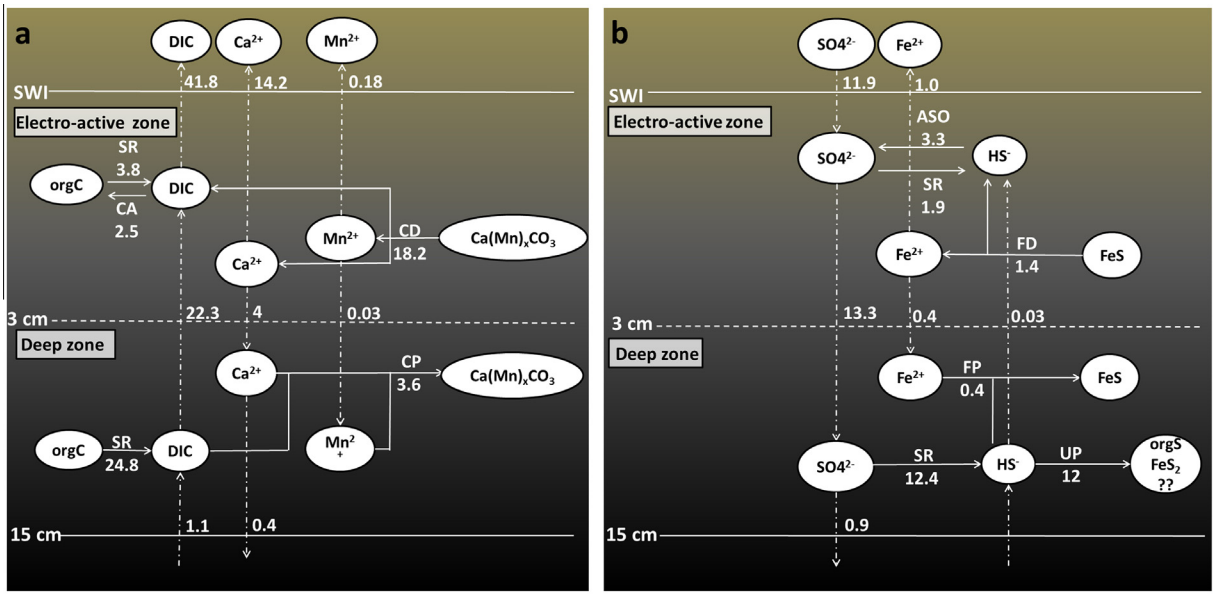

Fig. 8. Mass budget of the geochemical cycling of (a) Ca, Mn and C and (b) Fe and S in the upper 15 cm of sediment at the field site. Solid lines represent chemical reactions, dashed lines denote transport pathways (diffusion + ionic drift). Values given are the mean values of the rates and fluxes estimated for January, March and May 2014. SWI = sediment–water interface, ASO = anodic sulfide oxidation, SR = sulfate reduction, FD = FeS dissolution, FP = FeS precipitation, CD = carbonate dissolution, CP = carbonate precipitation, UP = unknown process. The upper boundary of the sediment domain is the SWI, the depth limit of the electro-active zone is located at 3 cm depth and the lower boundary of the sediment domain is located at 15 cm depth.

is comparable to the average Ca/Mn ratio of marine carbonates, which is typically around 50 (Burdige, 2006). In our data, we did not find any evidence for calcium carbonate precipitation near the sediment surface, as previously observed by Risgaard-Petersen et al. (2012). This is probably due to two reasons; (i) Carbonate precipitation does occur, but the resolution of the Ca^{2+} and Mn^{2+} profiles in the oxic zone is too coarse to reliably determine (co)precipitation by PROFILE analysis. (ii) Carbonate precipitation does not occur, as bottom currents transport the free calcium and manganese ions immediately away out of the diffusive boundary layer. Calcium fluxes out of the sediment (corrected for ionic drift and assuming no precipitation) ranged from 9.2 ± 2.4 to 18.2 ± 2.3 mmol m^{-2} d^{-1} (Table 3), which is a factor of 2–4 lower than observed by Rao et al. (2016), who measured Ca^{2+} effluxes between 8.2 and 48 mmol m^{-2} d^{-1} in incubation experiments. This difference can be explained by the difference in the e-SOx rate, where the laboratory sediments experienced higher e-SOx rates and hence a stronger acidification of the suboxic zone, inducing stronger carbonate dissolution.

As already discussed above, e-SOx has the potential to accelerate the release of Mn^{2+} from coastal sediments and thus could be an important input source of Mn^{2+} to the open ocean (Rao et al. (2016). As for Ca^{2+}, the Mn^{2+} fluxes here (0.14 ± 0.03–0.23 ± 0.04 mmol m^{-2} d^{-1}) are a factor of 2–4 lower than the Mn^{2+} fluxes (0.24–0.72 mmol m^{-2} d^{-1}) observed in laboratory experiments (Rao et al., 2016). The fluxes observed at the field site still fall within the upper range of previously measured manganese fluxes in coastal sediments (Aller, 1994; Thamdrup et al., 1994).

4.8. An integrated budget of carbon and sulfur cycling

The various reaction rates and fluxes discussed above were used to construct an integrated model of carbon and sulfur cycling at the Station 130 field site (Fig. 8, rates are given in Table 4). To this end, we divided the upper sediment into two zones. The upper box comprises the electro-active zone, which spans the suboxic zone and ranges from the sediment–water interface down to 3 cm depth. The second zone comprises the deeper sediment which extends down to 15 cm depth. Our model assumes a steady state for all pore water solutes (i.e. the sum of production and incoming fluxes must balance the sum of consumption and outgoing fluxes).

The carbon cycle is depicted in Fig 8a. In the electro-active zone, DIC is being produced by two pathways: (i) the dissolution of carbonate minerals, promoted by the low pH conditions induced by e-SOx (13.9 mmol C m^{-2} d^{-1}), and (ii) the mineralization of organic matter by sulfate reduction (4.2 mmol C m^{-2} d^{-1}). There is likely also a small DIC consumption (2.5 mmol C m^{-2} d^{-1}), as e-SOx has been linked to strong chemo-autotrophy (Vasquez-Cardenas et al., 2015). In the deeper zone, there is a small influx of DIC from deeper horizons (1.1 mmol C m^{-2} d^{-1}) and a large production through mineralization (24.8 mmol C m^{-2} d^{-1}), of which part is consumed by carbonate precipitation (3.6 mmol C m^{-2} d^{-1}), leading to an upward DIC flux of 22.3 mmol C m^{-2} d^{-1} to the electro-active zone. Overall, this

Table 4
Reaction equation set used in the carbon and sulfur budget. Two zones are delineated: an electro-active zone where e-SOx is the dominant sulfur cycling reaction, and a deeper zone where sulfate reduction is the dominant sulfur cycling reaction. Abbreviations are used in Fig. 8. Values represent (mean ± 1 s.d.) of depth profiles in replicate cores.

Process	Abbreviation	Reaction equation	Units	January	March	May
Top zone						
Cathodic oxygen consumption	COC	$4H^+ + 4e^- + O_2 \rightarrow 2H_2O$	mmol m^{-2} d^{-1}	6.6 ± 0.7	NA	5.8 ± 4.4
Anodic sulfide oxidation	ASO	$HS^- + 4H_2O \rightarrow SO_4^{2-} + 9H^+ + 8e^-$	mmol m^{-2} d^{-1}	3.3 ± 0.4	NA	2.9 ± 2.2
Sulfate reduction	SR	$2CH_2O + SO_4^{2-} \rightarrow 2HCO_3^- + HS^- + H^+$	mmol m^{-2} d^{-1}	2.3 ± 0.2	4.6 ± 0.7	2.6 ± 1.6
Iron sulfide dissolution	FD	$FeS + H^+ \rightarrow Fe^{2+} + HS^-$	mmol m^{-2} d^{-1}	1.6 ± 0.9	1.2 ± 0.2	0.7 ± 0.2
Carbonate dissolution	CD	$CaMn_{xCO_3} + H^+ \rightarrow Ca^{2+} + xMn^{2+} + HCO_3^-$	mmol m^{-2} d^{-1}	12 ± 7	22 ± 5	6.8 ± 3.0
Bottom zone						
Sulfate reduction	SR	$2CH_2O + SO_4^{2-} \rightarrow 2HCO_3^- + HS^- + H^+$	mmol m^{-2} d^{-1}	23.5 ± 7.5	22.6 ± 1.4	10.0 ± 3.4
Iron sulfide precipitation	FP	$Fe^{2+} + HS^- \rightarrow FeS + H^+$	mmol m^{-2} d^{-1}	0.6 ± 0.3	0.34 ± 0.02	0.4 ± 0.8
Carbonate precipitation	CD	$Ca^{2+} + xMn^{2+} + HCO_3^- \rightarrow CaMn_{xCO_3} + H^+$	mmol m^{-2} d^{-1}	4.7 ± 0.8	3.9 ± 1.3	2.2 ± 0.6

leads to a DIC efflux from the sediment of 37.9 mmol C m^{-2} d^{-1}, of which 73% results from net mineralization and 27% is due to the net carbonate dissolution. This flux is comparable to the previously measured efflux of DIC at Station 130 (66 ± 18 mmol C m^{-2} d^{-1}) by Braeckman et al. (2014). These results indicate that the presence of cable bacteria in coastal sediments has the potential to substantially increase the DIC efflux of coastal sediments, and will hinder the preservation and burial of carbonate phases.

A similar well-constrained model is developed for the sulfur cycle (Fig. 8b). In the electro-active zone, there is a strong influx of SO_4^{2-} from the bottom water (12.5 mmol S m^{-2} d^{-1}), of which a small fraction is used for sulfate reduction (2.1 mmol S m^{-2} d^{-1}). However, there is a net production of sulfate in the electro-active zone, as more sulfate is produced by e-SOx (3.3 mmol S m^{-2} d^{-1}). This then leads to a large downward flux of sulfate (13.7 mmol m^{-2} d^{-1}) to the deep zone, were most is consumed by sulfate reduction (12.4 mmol S m^{-2} d^{-1}) and a small efflux of SO_4^{2-} (1.3 mmol S m^{-2} d^{-1}) proceeds towards deeper layers. In the deep zone, sulfate reduction supplies 12.4 mmol m^{-2} d^{-1} of free sulfide, from which only 0.4 mmol m^{-2} d^{-1} is consumed by FeS precipitation. As the upward flux of free sulfide from the deep zone to the electro-active zone is negligible, there must be a large unknown sink for free sulfide (>12 mmol m^{-2} d^{-1}, as we do not account for the sulfide flux from deeper layers). The existence of such a large sulfur sink is clear, given the strong depletion of the sulfate pore water profile at depth, while at the same time, there is only a very small accumulation of free sulfide in the pore water. However, the nature of this free sulfide sink is puzzling, and could be linked to the formation of pyrite or the incorporation of sulfide in organic molecules (Brüchert and Pratt, 1996). However at present, we do not have sufficient data to identify its true nature, and hence further research is needed to identify this important sulfide sink.

5. CONCLUSIONS

Electrogenic sulfur oxidation occurs in marine sediments, both under laboratory conditions (Nielsen et al., 2010; Pfeffer et al., 2012) as well as *in situ* (Malkin et al., 2014). Previous laboratory incubation experiments have documented the effect of e-SOx on carbon, iron and sulfur cycling (Risgaard-Petersen et al., 2012; Rao et al., 2016), and here we present the first *in situ* study of e-SOx. The spatial separation of oxygen reduction and sulfur oxidation generates a characteristic geochemical signature and exerts a strong influence on the pore water geochemistry (Risgaard-Petersen et al., 2012; Meysman et al., 2015; Rao et al., 2016). Furthermore, the spatial segregation of two redox processes generates an electrical field in the upper 3–5 cm of the sediment column, which has a strong impact on the fluxes of charged species in the pore water (Risgaard-Petersen et al., 2012). Our results show that this ionic drift effect is most important for Ca^{2+} and SO_4^{2-}, two double charged species that are abundant in the pore water, as it was responsible for ~30% of the efflux for Ca^{2+} and up to 75% of the influx of SO_4^{2-}. For the less abundant species, the ionic drift effect ranged from >10% to 15%.

Previous studies of the Belgian Coastal Zone have focused on the influence of macrofauna (Braeckman et al., 2014) or the fate of trace metals in the sediment (Gao et al., 2009). Here we have presented the first process rates of early diagenesis in the Belgian Coastal Zone. Sulfate reduction is responsible for close to 100% of organic matter oxidation, while ~40% of the Diffusive Oxygen Uptake was consumed by Cathodic Oxygen Reduction and the other 60% is probably consumed by oxidation of upward diffusing reduced species (e.g. Fe^{2+}, Mn^{2+}) or aerobic mineralization.

Our results show that e-SOx influences coastal sediment in a direct way by scavenging sulfide from the upper 3–5 cm of the sediment column and generating an electrical field throughout the same zone, but also in an indirect manner by accelerating carbonate and sulfide mineral dissolution due to the consumption of alkalinity. This will potentially impact the long-term sulfur and carbon cycle, by hindering the formation of those minerals, and generating a stronger benthic DIC flux. Furthermore, the effect of e-SOx on iron and manganese cycling also suggests that trace metals are potentially influenced by this mode of sulfur oxidation, which is something that could be targeted in future studies.

ACKNOWLEDGEMENTS

The research leading to these results has received funding from the European Research Council under the European Union's Seventh Framework Programme (FP/2007-2013) through ERC Grant 306933 (FJRM) and was financially supported by Research Foundation Flanders (PhD Fellowship to SVDV and a PostDoc Fellowship to YG).

The authors would like to thank the crew of the RV Simon Stevin and the Flanders Marine Institute (VLIZ) for the assistance and financial support during the field campaigns, the analytical lab of the NIOZ for the analysis of the pore water and sediment samples and Tanja Stratmann and Angelina Smilenova for assistance during sampling and sample processing.

APPENDIX. SUPPLEMENTARY DATA

Supplementary data associated with this article can be found, in the online version, at http://dx.doi.org/10.1016/j.gca.2016.08.038.

REFERENCES

Aller R. C. (1994) The sedimentary Mn cycle in Long Island Sound: its role as intermediate oxidant and the influence of bioturbation, O2, and Corg flux on diagenetic reaction balances. *J. Mar. Res.* **52**, 259–295.

Aller R.C. (2014) Sedimentary Diagenesis, Depositional Environments, and Benthic Fluxes. In Treatise on Geochemistry 2nd Edition, Elsevier, 293–334.

Aminot A., Kérouel R. and Coverly S.C. (2009) Chapter 8: nutrients in seawater using segmented flow analysis. In Practical Guidelines for the Analysis of Seawater. CRC Press. Wurl O. (Ed.).

Berg P., Risgaard-Petersen N. and Rysgaard S. (1998) Interpretation of measured concentration profiles in the sediment pore water. *Limnol. Oceanogr.* **43**, 1500–1510.

Bottrell S. H. and Newton R. F. (2006) Reconstruction of changes in global sulfur cycling from marine sulfate isotopes. *Earth Sci. Rev.* **75**, 56–83.

Boudreau B. P. (1997) *Diagenetic Models and Their Implementation*. Springer.

Boudreau B. P. and Meysman F. J. R. (2006) Predicted tortuosity of muds. *Geology* **34**, 693–696.

Boudreau B. P., Mucci A., Sundby B., Luther G. W. and Silverberg N. (1998) Comparative diagenesis at three sites on the Canadian continental margin. *J. Mar. Res.* **56**, 1259–1284.

Braeckman U., Foshtomi M. Y., Van Gansbeke D., Meysman F., Soetaert K., Vinckx M. and Vanaverbeke J. (2014) Variable importance of macrofaunal functional biodiversity for biogeochemical cycling in temperate coastal sediment. *Ecosystems*. http://dx.doi.org/10.1007/s10021-014-9755-7.

Brüchert V. and Pratt L. M. (1996) Contemporaneous early diagenetic formation of organic and inorganic sulfur in estuarine sediments from St. Andrew Bay, Florida, USA. *Geochim. Cosmochim. Acta* **60**, 2325–2332.

Brzezinski M. A. (1985) The Si:C:N ratio of marine diatoms: interspecific variability and the effect of some environmental variables. *J. Phycol.* **21**, 347–357.

Burdige D. J. (2006) *Geochemistry of Marine Sediments*. Princeton University Press.

Burdorf L. D. W., Hidalgo-Martinez S., Cook P. L. M. and Meysman F. J. R. (2016) Long-distance electron transport by cable bacteria in mangrove sediments. *Mar. Ecol. Prog. Ser.* **545**, 1–8.

Burton E. D., Sullivan L. A., Bush R. T., Johnston S. G. and Keene A. F. (2008) A simple and inexpensive chromium-reducible sulfur method for acid-sulfate soils. *Appl. Geochem.* **23**, 2759–2766.

Canfield D. E., Raiswell R., Westrich J. T., Reaves C. M. and Berner R. A. (1986) The use of chromium reduction in the analysis of reduced inorganic sulfur in sediments and shales. *Chem. Geol.* **54**, 149–155.

Canfield D. E., Thamdrup B. and Hansen J. W. (1993) The anaerobic degradation of organic matter in Danish coastal sediments: iron reduction, manganese reduction and sulfate reduction. *Geochim. Cosmochim. Acta* **57**, 3867–3883.

Cornwell J. C. and Morse J. W. (1987) The characterization of iron sulfide minerals in anoxic marine sediments. *Mar. Chem.* **22**, 193–206.

Crompton T.R. (1989) Chapter 4: Metals. In: Analysis of Seawater, Butterworths & Co, 74–215.

Damgaard L. R., Risgaard-Petersen N. and Nielsen L. P. (2014) Electric potential microelectrode for studies of electrobiogeophysics. *J. Geophys. Res. Biogeosci.* **119**. http://dx.doi.org/10.1002/2014JG002665.

Dickson A. G., Afghan J. D. and Anderson G. C. (2003) Reference materials for oceanic CO_2 analysis: a method for the certification of total alkalinity. *Mar. Chem.* **80**, 185–197.

Dickson A.G., Sabine C.L. and Christian J.R. (Eds.). (2007) Guide to best practices for ocean CO_2 measurements. PICES Special Publication. 3, pp 191.

Dixit S., Van Cappellen P. and Johan van Bennekom A. (2001) Processes controlling solubility of biogenic silica and pore water build-up of silicic acid in marine sediments. *Mar. Chem.* **73**, 333–352.

Dunne J. P., Sarmiento J. L. and Gnanadesikan A. (2007) A synthesis of global particle export from the surface ocean and cycling through the ocean interior and on the seafloor. *Global Biogeochem. Cycles* **21**. http://dx.doi.org/10.1029/2006GB002907.

Finster K., Liesack W. and Thamdrup B. (1998) Elemental sulfur and thiosulfate disproportionation by *Desulfocapsa sulfoexigens* sp. Nov., a new anaerobic bacterium isolated from marine surface sediment. *Appl. Environ. Microb.* **64**, 119–125.

Gao Y., Lesven L., Gillan D., Sabbe K., Billon G., De Galan S., Elskens M., Baeyens W. and Leermakers M. (2009) Geochemical behavior of trace elements in sub-tidal marine sediments of the Belgian coast. *Mar. Chem.* **117**, 88–96.

Gorby Y. A., Yanina S., McLean J. S., Rosso K. M., Moyles D., Dohnalkova A., Beveridge T. J., Chang I. S., Kim B. H., Kim K. S., Culley D. E., Reed S. B., Romine M. F., Saffarini D. A., Hill E. A., Shi L., Elias D. A., Kennedy D. W., Pinchuk G., Watanabe K., Ishii S. I., Logan B., Nealson K. H. and Fredrickson J. K. (2006) Electrically conductive bacterial nanowires produced by *Shewanella oneidensis* strain MR-1 and other microorganisms. *Proc. Natl. Acad. Sci. U.S.A.* **103**, 11358–11363.

Gros N., Camões M. F., Oliveira C. and Silva M. C. R. (2008) Ionic composition of seawaters and derived saline solutions determined by ion chromatography and its relation to other water quality parameters. *J. Chromatogr. A* **1210**(1), 92–98.

ISO 12914:2012 – Soil quality — Microwave-assisted extraction of the aqua regia soluble fraction for the determination of elements – https://www.iso.org/obp/ui/#iso:std:iso:12914:ed-1:v1:en.

Jorgensen B. B. (1982) Mineralization of organic matter in the seabed – the role of sulfate reduction. *Nature* **296**, 643–645.

Kato S., Nakamura R., Kai F., Watanabe K. and Hashimoto K. (2010) Respiratory interactions of soil bacteria with (semi)conductive iron-oxide minerals. *Environ. Microbiol.* **12**, 3114–3123.

Lancelot C., Spitz Y., Gypens N., Ruddick K., Bequevort S., Rousseau V., Lacroix G. and Billen G. (2005) Modelling diatom and Phaeocystis blooms and nutrient cycles in the Southern Bight of the North Sea: the MIRO model. *Mar. Ecol. Prog. Ser.* **289**, 63–78.

Larsen S., Nielsen L. P. and Schramm A. (2015) Cable bacteria associated with long-distance electron transport in New England salt marsh sediment. *Environ. Microbiol. Rep.* **7**, 175–179.

Logan B. E. and Rabaey K. (2012) Conversion of wastes into bioelectricity and chemicals by using microbial electrochemical technologies. *Science* **337**, 686–690.

Lovley D. R. (2008) Extracellular electron transfer: wires, capacitors, iron lungs, and more. *Geobiology* **6**, 225–231.

Madison A. S., Tebo B. M. and Luther, III, G. W. (2011) Simultaneous determination of soluble manganese(III), manganese(II) and total manganese in natural (pore)waters. *Talanta* **84**, 374–381.

Malkin S. Y. and Meysman F. J. R. (2015) Rapid redox signal transmission by "Cable Bacteria" beneath a photosynthetic biofilm. *Appl. Environ. Microbiol.* **81**, 948–956.

Malkin S. Y., Rao A. M. F., Seitaj D., Vasquez-Cardenas D., Zetsche E., Boschker H. T. S. and Meysman F. J. R. (2014) Natural occurrence of microbial sulfur oxidation by long-range electron transport in the seafloor. *ISME J.* **8**(9), 1843–1854.

Manz W., Amann R., Ludwig W., Wagner M. and Schleifer K. H. (1992) Phylogenetic oligeodeoxynucleotide probes for the major subclasses of proteobacteria: problems and solutions. *Syst. Appl. Microbiol.* **15**, 593–600.

Marzocchi U., Trojan D., Larsen S., Louise Meyer R., Revsbech N. P., Schramm A., Nielsen L. P. and Risgaard-Petersen N. (2014) Electrical coupling between distant nitrate reduction and sulfide oxidation in marine sediment. *ISME J.* **8**, 1682–1690.

McCave I. N. (1986) Evaluation of laser-diffraction-size analyzer for use with natural sediments. *J. Sed. Res.* **54**(4), 561–564.

Meysman F. J. R., Risgaard-Petersen N., Malkin S. Y. and Nielsen L. P. (2015) The geochemical fingerprint of microbial long-distance transport in the seafloor. *Geochim. Cosmochim. Acta* **152**, 122–142.

Millero F. J., Plese T. and Fernandez M. (1988) The dissociation of hydrogen sulfide in seawater. *Limnol. Oceanogr.* **33**(2), 269–274.

Nielsen L. P. and Risgaard-Petersen N. (2015) Rethinking sediment biogeochemistry after the discovery of electric currents. *Ann. Rev. Mar. Sci.* **7**, 425–442.

Nielsen L. P., Risgaard-Petersen N., Fossing H., Christensen P. B. and Sayama M. (2010) Electric currents couple spatially separated biogeochemical processes in marine sediment. *Nature* **463**, 1071–1074.

Nieuwenhuize J., Maas Y. E. M. and Middelburg J. J. (1994) Rapid analysis of organic carbon and nitrogen in particulate materials. *Mar. Chem.* **45**, 217–224.

Ntarlagiannis D., Atekwana E. A., Hill E. A. and Gorby Y. (2007) Microbial nanowires: is the subsurface "hardwired"? *Geophys. Res. Lett.* **34**. http://dx.doi.org/10.1029/2007GL030426.

Pfeffer C., Larsen S., Song J., Dong M., Besenbacher F., Meyer R. L., Kjeldsen K. U., Schreiber L., Gorby Y. A., El-Naggar M. Y., Leung K. M., Schramm A., Risgaard-Petersen N. and Nielsen L. P. (2012) Filamentous bacteria transport electrons over centimetre distances. *Nature* **491**, 218–221.

Poussel E., Mermet J. M. and Samuel O. (1993) Simple experiments for control, evaluation and diagnosis of inductively coupled plasma sequential systems. *Spectrochim. Acta* **48**, 743–755.

Rao A. M. F., Malkin S. Y., Hidalgo-Martinez S. and Meysman F. J. R. (2016) The impact of electrogenic sulfur oxidation on elemental cycling and solute fluxes in coastal sediment. *Geochim. Cosmochim. Acta* **172**, 265–286.

Redfield A. C. (1934) On the proportions of organic derivations in sea water and their relation to the composition of plankton. In *James Johnstone Memorial Volume* (ed. R. J. Daniel). University Press of Liverpool, pp. 177–192.

Risgaard-Petersen N., Revil A., Meister P. and Nielsen L. P. (2012) Sulfur, iron-, and calcium cycling associated with natural electric currents running through marine sediment. *Geochim. Cosmochim. Acta* **92**, 1–13.

Risgaard-Petersen N., Damgaard R. L., Revil A. and Nielsen L. P. (2014) Mapping electron sources and sinks in a marine biogeobattery. *J. Geophys. Res. Biogeosci.* **119**, 1475–1486.

Schauer R., Risgaard-Petersen N., Kjeldsen K. U., Tataru Bjerg J. J., Jorgensen B. B., Schramm A. and Nielsen L. P. (2014) Succession of cable bacteria and electric currents in marine sediment. *ISME J.* **8**, 1314–1322.

Severmann S., McManus J., Berelson W. M. and Hammond D. E. (2010) The continental shelf benthic iron flux and its isotope composition. *Geochim. Cosmochim. Acta* **74**, 3984–4004.

Soetaert K., Petzoldt T. and Meysman F. (2010) marelac: Tools for Aquatic Sciences. R Package Version 2.1. http://CRAN.R-project.org/package=marelac.

Stoll M. H. C., Bakker K., Nobbe G. H. and Haese R. R. (2001) Continuous-flow analysis of dissolved inorganic carbon content in seawater. *Anal. Chem.* **73**, 4111–4116.

Thamdrup B., Finster K., Würgler Hansen J. and Bak F. (1993) Bacterial disproportionation of elemental sulfur coupled to chemical reduction of iron and manganese. *App. Environ. Microb.* **59**, 101–108.

Thamdrup B., Fossing H. and Jorgensen B. B. (1994) Manganese, iron and sulfur cycling in a coastal marine sediment, Aarhus Bay, Denmark. *Geochim. Cosmochim. Acta.* **58**(23), 5115–5129.

Trojan D., Schreiber L, Bjerg JT, Boggild A, Yang T, Kjeldsen KU and Schramm A. (2016) A taxonomic framework for cable bacteria and proposal of the candidate genera Electrothrix and Electronema. Syst. Appl. Microbiol. http://dx.doi.org/10.1016/j.syapm.2016.05.006.

van Beusekom J.E.E. and Diel-Christiansen S. (1994). A synthesis of phyto- and zooplankton dynamics in the North Sea environment. WWF—World Wide Fund For Nature 148.

Van Lancker V., Deleu S., Bellec V., Le Bot S., Verfaillie E., Fettweis M., Van den Eynde D., Francken F., Pison V., Wartel S., Monballiu J., Portilla J., Lanckneus J., Moerkerke G. & Degraer S. (2004) Management, research and budgeting of aggregates in shelf seas related to end-users (Marebasse). Scientific Report Year 2. Belgian Science Policy, 144 p.

Vasquez-Cardenas D., van de Vossenberg J., Polerecky L., Malkin S. Y., Schauer R., Hidalgo-Martinez S., Confurius V., Middelburg J. J., Meysman F. J. R. and Boschker H. T. S. (2015) Microbial carbon metabolism associated with electrogenic sulphur oxidation in coastal sediments. *ISME J.*. http://dx.doi.org/10.1038/ismej.2015.10.

Viollier E., Inglett P. W., Hunter K., Roychoudhurry A. N. and Van Cappellen P. (2000) The ferrozine method revisited: Fe(II)/Fe(III) determination in natural waters. *Appl. Geochem.* **15**, 785–790.

Vlaamse Hydrografie. (2012) Kaart D11 Noordzee Vlaamse Banken. Van Gravelines tot Oostkapelle. 1:100.000. Agentschap voor Maritieme Dienstverlening en Kust. Afdeling Kust. Vlaamse Hydrografie.

Wijsman J. W. M., Middelburg J. J. and Heip C. H. R. (2001) Reactive iron in Black Sea sediments: implications for iron cycling. *Mar. Geol.* **172**, 167–180.

Associate editor: Ruth Blake